

This is the accepted manuscript made available via CHORUS. The article has been published as:

**Measurement of target and double-spin asymmetries for the  $e[\overrightarrow{over}]p[\overrightarrow{over}] \rightarrow e\pi^{\{+}\}(n)$  reaction in the nucleon resonance region at low  $Q^{\{2\}}$**

X. Zheng *et al.* (CLAS Collaboration)

Phys. Rev. C **94**, 045206 — Published 19 October 2016

DOI: [10.1103/PhysRevC.94.045206](https://doi.org/10.1103/PhysRevC.94.045206)

1 **Measurement of Target and Double-spin Asymmetries for the  $\vec{e}p \rightarrow e\pi^+(n)$  Reaction in the Nucleon**  
2 **Resonance Region at Low  $Q^2$**

3 X. Zheng,<sup>1</sup> K.P. Adhikari,<sup>2,3</sup> P. Bosted,<sup>4</sup> A. Deur,<sup>4,1</sup> V. Drozdov,<sup>5,6</sup> L. El Fassi,<sup>2,7</sup> Hyekoo Kang,<sup>8</sup> K. Kovacs,<sup>1</sup> S. Kuhn,<sup>3</sup>  
4 E. Long,<sup>9</sup> S.K. Phillips,<sup>9</sup> M. Ripani,<sup>5</sup> K. Slifer,<sup>9</sup> L.C. Smith,<sup>1</sup> D. Adikaram,<sup>3</sup> Z. Akbar,<sup>10</sup> M.J. Amaryan,<sup>3</sup> S.  
5 Anefalos Pereira,<sup>11</sup> G. Asryan,<sup>12</sup> H. Avakian,<sup>4</sup> R.A. Badui,<sup>13</sup> J. Ball,<sup>14</sup> N.A. Baltzell,<sup>4,15</sup> M. Battaglieri,<sup>5</sup> V. Batourine,<sup>4</sup>  
6 I. Bedlinskiy,<sup>16</sup> A.S. Biselli,<sup>17,18</sup> W.J. Briscoe,<sup>19</sup> S. Bültmann,<sup>3</sup> V.D. Burkert,<sup>4</sup> D.S. Carman,<sup>4</sup> A. Celentano,<sup>5</sup> S. Chandavar,<sup>20</sup>  
7 G. Charles,<sup>21</sup> J.-P. Chen,<sup>4</sup> T. Chetry,<sup>20</sup> Seonho Choi,<sup>8</sup> G. Ciullo,<sup>22</sup> L. Clark,<sup>23</sup> L. Colaneri,<sup>24,25</sup> P.L. Cole,<sup>26</sup> N. Compton,<sup>20</sup>  
8 M. Contalbrigo,<sup>22</sup> V. Crede,<sup>10</sup> A. D Angelo,<sup>24,25</sup> N. Dashyan,<sup>12</sup> R. De Vita,<sup>5</sup> E. De Sanctis,<sup>11</sup> C. Djalali,<sup>15</sup> G.E. Dodge,<sup>3</sup>  
9 R. Dupre,<sup>21</sup> H. Egiyan,<sup>4,9</sup> A. El Alaoui,<sup>27</sup> L. Elouadrhiri,<sup>4</sup> P. Eugenio,<sup>10</sup> E. Fanchini,<sup>5</sup> G. Fedotov,<sup>15,6</sup> R. Fersch,<sup>28</sup> A. Filippi,<sup>29</sup>  
10 J.A. Fleming,<sup>30</sup> N. Gevorgyan,<sup>12</sup> Y. Ghandilyan,<sup>12</sup> G.P. Gilfoyle,<sup>31</sup> K.L. Giovanetti,<sup>32</sup> F.X. Girod,<sup>4,14</sup> C. Gleason,<sup>15</sup>  
11 E. Golovach,<sup>6</sup> R.W. Gothe,<sup>15</sup> K.A. Grif oen,<sup>33</sup> M. Guidal,<sup>21</sup> N. Guler,<sup>3</sup> L. Guo,<sup>13,4</sup> C. Hanretty,<sup>1</sup> N. Harrison,<sup>4</sup>  
12 M. Hattawy,<sup>7</sup> K. Hicks,<sup>20</sup> M. Holtrop,<sup>9</sup> S.M. Hughes,<sup>30</sup> Y. Ilieva,<sup>15,19</sup> D.G. Ireland,<sup>23</sup> B.S. Ishkhanov,<sup>6</sup> E.L. Isupov,<sup>6</sup>  
13 D. Jenkins,<sup>34</sup> H. Jiang,<sup>15</sup> H.S. Jo,<sup>21</sup> S. Joosten,<sup>35</sup> D. Keller,<sup>1</sup> G. Khachatryan,<sup>12</sup> M. Khandaker,<sup>26,36</sup> A. Kim,<sup>37</sup>  
14 W. Kim,<sup>38</sup> F.J. Klein,<sup>39</sup> V. Kubarovskiy,<sup>4,40</sup> L. Lanza,<sup>24,25</sup> P. Lenisa,<sup>22</sup> K. Livingston,<sup>23</sup> I. J. D. MacGregor,<sup>23</sup>  
15 N. Markov,<sup>37</sup> B. McKinnon,<sup>23</sup> M. Mirazita,<sup>11</sup> V. Mokeev,<sup>4,6</sup> A. Movsisyan,<sup>22</sup> E. Munevar,<sup>4,19</sup> C. Munoz Camacho,<sup>21</sup> G.  
16 Murdoch,<sup>23</sup> P. Nadel-Turronski,<sup>4,39</sup> L.A. Net,<sup>15</sup> A. Ni,<sup>38</sup> S. Niccolai,<sup>21</sup> G. Niculescu,<sup>32</sup> I. Niculescu,<sup>32</sup> M. Osipenko,<sup>5</sup>  
17 A.I. Ostrovodov,<sup>10</sup> M. Paolone,<sup>35</sup> R. Paremuzyan,<sup>9</sup> K. Park,<sup>4,38</sup> E. Pasyuk,<sup>4</sup> P. Peng,<sup>1</sup> S. Pisano,<sup>11</sup> O. Pogorelko,<sup>16</sup>  
18 J.W. Price,<sup>41</sup> A.J.R. Puckett,<sup>37</sup> B.A. Raue,<sup>13,4</sup> A. Rizzo,<sup>24,25</sup> G. Rosner,<sup>23</sup> P. Rossi,<sup>4,11</sup> P. Roy,<sup>10</sup> F. Sabatié,<sup>14</sup>  
19 C. Salgado,<sup>36</sup> R.A. Schumacher,<sup>18</sup> Y.G. Sharabian,<sup>4</sup> Iu. Skorodumina,<sup>15,6</sup> G.D. Smith,<sup>30</sup> D. Sokhan,<sup>23</sup> N. Sparveris,<sup>35</sup>  
20 I. Stankovic,<sup>30</sup> I.I. Strakovsky,<sup>19</sup> S. Strauch,<sup>15,19</sup> M. Taiuti,<sup>5,42</sup> Ye Tian,<sup>15</sup> M. Ungaro,<sup>4,37</sup> H. Voskanyan,<sup>12</sup> E. Voutier,<sup>21</sup>  
21 N.K. Walford,<sup>39</sup> D.P. Watts,<sup>30</sup> X. Wei,<sup>4</sup> L.B. Weinstein,<sup>3</sup> M.H. Wood,<sup>43,15</sup> N. Zachariou,<sup>30</sup> J. Zhang,<sup>4</sup> and I. Zonta<sup>24,25</sup>

(The CLAS Collaboration)

<sup>1</sup>University of Virginia, Charlottesville, Virginia 22901, USA

<sup>2</sup>Mississippi State University, Mississippi State, Mississippi 39762, USA

<sup>3</sup>Old Dominion University, Norfolk, Virginia 23529, USA

<sup>4</sup>Thomas Jefferson National Accelerator Facility, Newport News, Virginia 23606, USA

<sup>5</sup>INFN, Sezione di Genova, 16146 Genova, Italy

<sup>6</sup>Skobeltsyn Institute of Nuclear Physics, Lomonosov Moscow State University, 119234 Moscow, Russia

<sup>7</sup>Argonne National Laboratory, Argonne, Illinois 60439, USA

<sup>8</sup>Seoul National University, Seoul, Korea

<sup>9</sup>University of New Hampshire, Durham, New Hampshire 03824, USA

<sup>10</sup>Florida State University, Tallahassee, Florida 32306, USA

<sup>11</sup>INFN, Laboratori Nazionali di Frascati, 00044 Frascati, Italy

<sup>12</sup>Yerevan Physics Institute, 375036 Yerevan, Armenia

<sup>13</sup>Florida International University, Miami, Florida 33199, USA

<sup>14</sup>CEA, Centre de Saclay, Irfu/Service de Physique Nucléaire, 91191 Gif-sur-Yvette, France

<sup>15</sup>University of South Carolina, Columbia, South Carolina 29208, USA

<sup>16</sup>Institute of Theoretical and Experimental Physics, Moscow, 117259, Russia

<sup>17</sup>Fair eld University, Fair eld, Connecticut 06824, USA

<sup>18</sup>Carnegie Mellon University, Pittsburgh, Pennsylvania 15213, USA

<sup>19</sup>The George Washington University, Washington, DC 20052, USA

<sup>20</sup>Ohio University, Athens, Ohio 5701, USA

<sup>21</sup>Institut de Physique Nucléaire, CNRS/IN2P3 and Université Paris Sud, Orsay, France

<sup>22</sup>INFN, Sezione di Ferrara, 44100 Ferrara, Italy, USA

<sup>23</sup>University of Glasgow, Glasgow G12 8QQ, United Kingdom

<sup>24</sup>INFN, Sezione di Roma Tor Vergata, 00133 Rome, Italy

<sup>25</sup>Università di Roma Tor Vergata, 00133 Rome Italy

<sup>26</sup>Idaho State University, Pocatello, Idaho 83209, USA

<sup>27</sup>Universidad Técnica Federico Santa Mar'a, Casilla 110-V Valpara'so, Chile

<sup>28</sup>Christopher Newport University, Newport News, Virginia 23606, USA

<sup>29</sup>INFN, Sezione di Torino, 10125 Torino, Italy

<sup>30</sup>Edinburgh University, Edinburgh EH9 3JZ, United Kingdom

<sup>31</sup>University of Richmond, Richmond, Virginia 23173, USA

<sup>32</sup>James Madison University, Harrisonburg, Virginia 22807, USA

<sup>33</sup>College of William and Mary, Williamsburg, Virginia 23187, USA

<sup>34</sup>Virginia Tech, Blacksburg, Virginia 24061, USA

<sup>35</sup>Temple University, Philadelphia, Pennsylvania 19122, USA

<sup>36</sup>Norfolk State University, Norfolk, Virginia 23504, USA

59 <sup>37</sup>*University of Connecticut, Storrs, Connecticut 06269, USA*  
 60 <sup>38</sup>*Kyungpook National University, Daegu 702-701, Republic of Korea*  
 61 <sup>39</sup>*Catholic University of America, Washington, D.C. 20064, USA*  
 62 <sup>40</sup>*Rensselaer Polytechnic Institute, Troy, New York 12180, USA*  
 63 <sup>41</sup>*California State University, Dominguez Hills, Carson, California 90747, USA*  
 64 <sup>42</sup>*Universita di Genova, Dipartimento di Fisica, 16146 Genova, Italy*  
 65 <sup>43</sup>*Canisius College, Buffalo, New York 14208, USA*

66 (Dated: September 22, 2016)

We report measurements of target- and double-spin asymmetries for the exclusive channel  $ep \rightarrow e^+(n)$  in the nucleon resonance region at Jefferson Lab using the CEBAF Large Acceptance Spectrometer (CLAS). These asymmetries were extracted from data obtained using a longitudinally polarized  $\text{NH}_3$  target and a longitudinally polarized electron beam with energies 1.1, 1.3, 2.0, 2.3 and 3.0 GeV. The new results are consistent with previous CLAS publications but are extended to a low  $Q^2$  range from 0.0065 to 0.35 (GeV  $c^2$ ). The  $Q^2$  access was made possible by a custom-built Cherenkov detector that allowed the detection of electrons for scattering angles as low as 6°. These results are compared with the unitary isobar models JANR and MAID, the partial-wave analysis prediction from SAID and the dynamic model DMT. In many kinematic regions our results, in particular results on the target asymmetry, help to constrain the polarization-dependent components of these models.

67 PACS numbers: 13.60.Lc, 13.88.+e, 14.20.Gk

## 68 I. PHYSICS MOTIVATION

69 The perturbative nature of the strong interaction at small  
 70 distances – often referred to as “asymptotic freedom” – was  
 71 established more than 30 years ago and provided strong sup-  
 72 port for Quantum Chromodynamics (QCD) to be accepted as  
 73 the correct theory for strong interactions [1, 2]. On the other  
 74 hand, calculations at long-distances are still beyond reach be-  
 75 cause of the non-perturbative nature at this scale. As a re-  
 76 sult, we are still far away from being able to describe the  
 77 strong force as it manifests itself in the structure of baryons  
 78 and mesons [3][4].

79 A fundamental approach to resolve this difficulty is to de-  
 80 velop accurate numerical simulations of QCD on the Lattice,  
 81 for recent reviews see [5, 6]. However Lattice QCD methods  
 82 are difficult to apply to light-quark systems such as the nu-  
 83 cleon. Alternatively, hadron models with effective degrees of  
 84 freedom have been constructed to interpret data. One example  
 85 is the chiral perturbation theory [7, 8], which is constrained  
 86 only by the symmetry properties of QCD. The constituent  
 87 quark model, though not fully understood, is one success-  
 88 ful example that works almost everywhere from hadron spec-  
 89 troscopy to deep inelastic scattering [9, 10]. Predictions for  
 90 the scattering amplitudes and polarization-dependent asym-  
 91 metries exist for many resonances within the framework of  
 92 the relativistic constituent quark model (RCQM) [11] and the  
 93 single quark transition model (SQTM) [12].

94 The comparison between these predictions and experimen-  
 95 tal results, on the other hand, is not straightforward. This  
 96 is because the experimentally measured cross sections and  
 97 asymmetries are usually complicated combinations of reso-  
 98 nant and non-resonant amplitudes and couplings, and their

99 interference terms. To compare with theories, partial wave  
 100 analyses are often used to extract these amplitudes and reso-  
 101 nance couplings from data. Once comparisons can be made,  
 102 data are used to provide inputs for constructing or adjusting  
 103 meson production mechanisms in theories and models, such  
 104 as proper treatment of the hadronic final state and implemen-  
 105 tation of the non-resonant part of the meson production am-  
 106 plitude. These mechanisms are usually not included in quark  
 107 models. Examples of phenomenological partial wave analyses  
 108 that can benefit from more data are MAID [13], JANR [14],  
 109 SAID [15], and the DMT [16] models. Electron-scattering  
 110 data used to test these calculations include primarily  $N \rightarrow N$   
 111 transition form factors and response functions for meson pro-  
 112 duction reactions obtained from Jefferson Lab (JLab), MAMI  
 113 and MIT-Bates. Recently, polarization observables such as  
 114 double spin asymmetries and target spin asymmetries for pion  
 115 electro-production from the proton have made the beam- and  
 116 target-helicity response functions accessible [17–20], provid-  
 117 ing a new approach to testing models and to a greater under-  
 118 standing of the baryon resonance structure. As an example,  
 119 the MAID model was based mostly on unpolarized data and  
 120 is only recently being tested extensively against double po-  
 121 larization asymmetries. In general, polarization observables  
 122 provide an important constraint on the understanding of the  
 123 underlying helicity response functions or interference terms  
 124 in  $N \rightarrow N$  and  $N \rightarrow N$  resonances.

125 Compared to the proton, existing data on neutron excitation  
 126 were particularly sparse. Neutron data have recently become  
 127 available from JLab [21, 22], which make it possible to test the  
 128 isospin structure of models such as RCQM and SQTM. The  
 129 neutron data will be valuable to the development of many phe-  
 130 nomenological analyses as well because they need to incorpo-  
 131 rate double polarization asymmetry data for all pion produc-  
 132 tion channels from both the proton and the neutron in order to  
 133 perform the full isospin decomposition.

134 In addition, data at very low  $Q^2$  values are often desired for  
 135 testing the chiral perturbation theory and to study the transi-  
 136 tion from virtual photons to the real photon point ( $Q^2 = 0$ ).  
 137 Here,  $Q^2$  is defined as  $Q^2 = q^2$ , where  $q = (q)$  is the

Current address: Thomas Jefferson National Accelerator Facility, Newport News, Virginia 23606, USA

Current address: Los Alamos National Laboratory, Los Alamos, New Mexico 87544, USA

138 four-momentum transferred from the incident electron to the  
139 target and

$$140 \quad \nu \equiv E - E' \quad (1)$$

141 with  $E$  and  $E'$  the incident and the scattered electron's energies, respectively. At low energy transfers  
142  $\nu < 2$  GeV the most prominent resonances are the  
143  $\Delta(1232)3/2^+$ ,  $N(1520)3/2^-$  and  $N(1680)5/2^+$  [11]. For  
144 the  $N(1520)3/2^-$  and  $N(1680)5/2^+$ , their amplitudes at  
145 large  $Q^2$  are determined by perturbative QCD and hadron heli-  
146 cility conservation. It is expected in this region that  $A^N \rightarrow 1$ ,  
147 where  $A^N$  is the virtual photon helicity asymmetry defined as:

$$149 \quad A^N = \frac{|A_{1/2}|^2 - |A_{3/2}|^2}{|A_{1/2}|^2 + |A_{3/2}|^2}, \quad (2)$$

150 with  $A_{1/2,3/2}$  the scattering amplitudes and the subscripts in-  
151 dicate the total spin projection of the virtual photon and the  
152 nucleon target along the virtual photon's momentum. How-  
153 ever, data using real photons show a strong helicity-3/2 dom-  
154 inance and  $A^N \rightarrow -1$  [23]. This indicates that  $A^N$  for these  
155 two resonances must cross zero at some intermediate  $Q^2$  and  
156 there have been calculations for the  $Q^2$ -dependence of  $A^N$   
157 from various models [11, 12, 24]. For pion electroproduc-  
158 tion, the double spin asymmetry is dominated by  $A^N$  [17] and  
159 thus data on this observable will allow us to test a possible  
160 sign flip for the  $N(1520)3/2^-$  and  $N(1680)5/2^+$  resonances.  
161 Data on the double spin asymmetry of pion photoproduc-  
162 tion have recently become available from the CBELSA/TAPS  
163 Collaboration [25] and are also expected from JLab experi-  
164 ments [26][27][28], all used the frozen spin target with a lon-  
165 gitudinal polarization and a circularly polarized photon beam.  
166 These photoproduction data will further test the transition to  
167 the real photon point.

### 168 A. Formalism for Pion Electroproduction

169 Figure 1 shows the kinematics of single pion production in  
170 the Born approximation: the electron transfers a virtual pho-  
171 ton  $\gamma^*$  of four-momentum  $q \equiv (\nu, \vec{q})$  to the target nucleon  $N$   
172 which forms a nucleon resonance. The resonance then decays  
173 into a pion and another particle  $X$ . Two planes are used to de-  
174 scribe this process: the scattering (leptonic) plane defined by  
175 the incoming and outgoing electrons' momenta  $\vec{k}$  and  $\vec{k}'$ , and  
176 the reaction (hadronic) plane defined by the momentum of the  
177 virtual photon  $\vec{q}$  and the momentum of the outgoing pion  $\vec{p}_\pi$ .  
178 The reaction is usually described in terms of  $Q^2$ , the invari-  
179 ant mass  $W$  of the  $\gamma^*N$  system (which is also the  $\pi X$  system),  
180 and two angles  $\theta^*$  and  $\phi^*$ . Here,  $\theta^*$  is the angle formed by  $\vec{q}$   
181 and  $\vec{p}_\pi$ , and  $\phi^*$  is the angle formed by rotating the leptonic  
182 plane to the hadronic plane. If one defines the  $\gamma^*N$  center  
183 of mass (CM) frame with  $\hat{z}$  pointing along  $\vec{q}$ ,  $\hat{y}$  along  $\vec{q} \times \vec{k}$ ,  
184 then  $\theta^*$  and  $\phi^*$  are the polar and the azimuthal angles of the  
185 emitted pion. The energy transfer is related to  $Q^2$  and  $W$  via

$$186 \quad \nu = \frac{W^2 + Q^2 - M^2}{2M}, \quad (3)$$

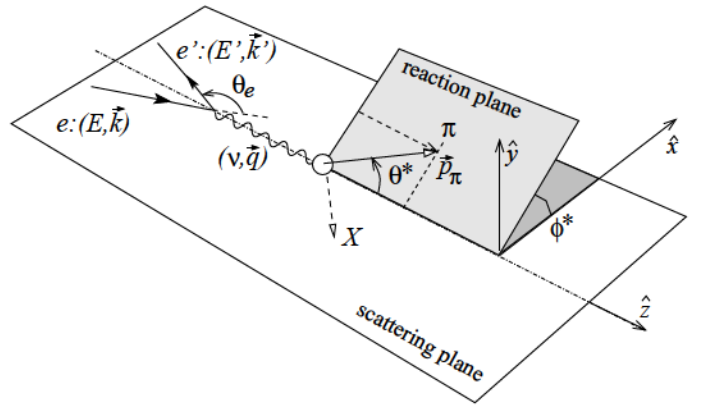


FIG. 1. Kinematics of single pion electro-production. The Lorentz boost associated with the transformation from the laboratory to the CM frame of the  $\gamma^* N$  system is along the momentum transfer  $\vec{q}$ , where the coordinates  $\hat{x}, \hat{y}, \hat{z}$  of the CM frame are defined in this picture.

187 with  $M$  the nucleon mass. The differential cross section for  
188 the reaction  $\bar{e}N \rightarrow e\pi(X)$  with longitudinally polarized beam  
189 and target can be written in the following form

$$190 \quad \frac{d^5\sigma_h}{dE_{e'}d\Omega_{e'}d\Omega_\pi^*} = \Gamma \frac{d\sigma_h}{d\Omega_\pi^*}, \quad (4)$$

191 with

$$192 \quad \frac{d\sigma_h}{d\Omega_\pi^*} = \frac{d\sigma_0}{d\Omega_\pi^*} + P_b \frac{d\sigma_e}{d\Omega_\pi^*} + P_t \frac{d\sigma_t}{d\Omega_\pi^*} + P_b P_t \frac{d\sigma_{et}}{d\Omega_\pi^*} \quad (5)$$

193 where  $P_b$  and  $P_t$  are respectively the polarizations of the elec-  
194 tron beam and the target along the beam direction,  $\sigma_0$  is the  
195 unpolarized cross section, and  $\sigma_e$ ,  $\sigma_t$  and  $\sigma_{et}$  are the polarized  
196 cross section terms when beam, target, and both beam and tar-  
197 get are polarized. Note that the differential cross sections on  
198 the right-hand side of Eq. (5) are defined in the CM frame of  
199 the  $\gamma^*N$  system, as indicated by the asterisk in the pion's solid  
200 angle. The virtual photon flux is

$$201 \quad \Gamma = \frac{\alpha k_\gamma^{\text{lab}}}{2\pi^2 Q^2} \frac{E'}{E} \frac{1}{1 - \epsilon}, \quad (6)$$

202 where  $\alpha$  is the electromagnetic coupling constant,  $k_\gamma^{\text{lab}} =$   
203  $(W^2 - M^2)/2M$  is the photon equivalent energy in the labo-  
204 ratory frame, i.e. the energy needed by a real photon to excite  
205 the nucleon to an invariant mass  $W$ . The virtual photon polar-  
206 ization is given by

$$207 \quad \epsilon = \left[ 1 + \frac{2|\vec{q}|^2}{Q^2} \tan^2 \frac{\theta_e}{2} \right]^{-1}, \quad (7)$$

208 where  $\theta_e$  is the angle between the incident and outgoing elec-  
209 trons in the laboratory frame. The  $Q^2$  can be calculated as

$$210 \quad Q^2 = 4EE' \sin^2 \frac{\theta_e}{2}. \quad (8)$$

211 To evaluate the pion's kinematics in the CM frame of the  
 212  $N$  system, we relate a laboratory-frame 4-momentum vec-  
 213 tor  $p$  to the CM-frame  $p_{cm}$  via a Lorentz boost with  
 214  $z q$  ( $+M$ ) and  $= (+M) W$ :

$$\begin{aligned} 215 \quad p_{cm}^0 &= p^0 & p^z \\ 216 \quad p_{cm}^x &= p^x \\ 217 \quad p_{cm}^y &= p^y \\ 218 \quad p_{cm}^z &= p^0 + p^z \end{aligned}$$

219 Specifically, we have for the virtual photon:

$$\begin{aligned} 220 \quad q_{cm} &= \frac{M}{W} q \\ 221 \quad q_{cm} &= \frac{M}{W} \frac{Q^2}{W} \end{aligned}$$

222 For the pion

$$\begin{aligned} 223 \quad E_{cm} &= (E - p \cos \theta) \\ 224 \quad p_{z,cm} &= (p \cos \theta - E) \end{aligned}$$

225 where  $\theta = \arccos[(q \cdot p) / (q \cdot p)]$  is the angle between the  
 226 pion momentum and  $q$  in the laboratory frame, and  $E$  is the  
 227 pion energy again in the laboratory frame. The polar angle of  
 228 the pion in the CM frame is given by

$$229 \quad \theta = \arccos \frac{p_{z,cm}}{E_{cm} / m^2} \quad (17)$$

230 where  $m$  is the pion mass. The azimuthal angle of the pion  
 231 is the same in the laboratory and the CM frame, given by

$$232 \quad \phi = \arccos \frac{a \cdot b}{a \cdot b} \quad (18)$$

233 with  $a = q - k$  and  $b = q - p$ . In this paper, the range of  
 234 is defined from 0 to  $2\pi$ , i.e. a shift of  $2\pi$  is added to  $\phi$  if the  
 235 result from Eq. (18) is negative.

236 The beam, target and double beam-target asymmetries are

$$237 \quad A_{UL} = \frac{e}{0} \quad (19)$$

$$238 \quad A_{UL} = \frac{t}{0} \quad (20)$$

$$239 \quad A_{LL} = \frac{et}{0} \quad (21)$$

240 where each cross section  $\sigma$  stands for the  $d\sigma/d\Omega$  of Eq. (5).

241 Note that we have adopted an extra minus sign in the defini-  
 242 tion of  $A_{LL}$  to be consistent with Eq. (2) and previous CLAS  
 243 publications [17–19].

244 In this paper, we report on results of both  $A_{UL}$  and  $A_{LL}$   
 245 extracted from the JLab CLAS EG4 [29, 30] data. The beam  
 246 asymmetry  $A_{UL}$  was also extracted from the data, but was  
 247 used only as a cross-check of the beam helicity and is not  
 248 presented here. These results are available for download from  
 249 the CLAS database.

## B. Previous Data

250 The first double-spin asymmetry for the  $^+n$  channel was  
 251 published based on the CLAS EG1a data with a 2.6 GeV  
 252 beam, for a  $Q^2$  range from 0.35 to 1.5  $(\text{GeV}/c)^2$  [17, 18]. The  
 253  $ep \rightarrow e p(\pi^0)$  channel was analyzed for the  $(1232)3/2^+$   
 254 region using the same dataset [19]. Similar analysis using the  
 255 CLAS EG1b data has been completed [20, 22], in which the  
 256 target and the double spin asymmetries were extracted from  
 257 both the  $ep \rightarrow e \pi^+(n)$  and  $en \rightarrow e \pi^- p$  channels using 1.6  
 258 to 5.7 GeV beams with  $Q^2$  as low as 0.1  $(\text{GeV}/c)^2$ .

## II. THE JLAB CLAS EG4 EXPERIMENT

260 The main physics goal of the CLAS EG4 experiment [29,  
 261 30] was to measure the inclusive spin structure functions on  
 262 the proton and the deuteron, and to extract the generalized  
 263 Gerasimov-Drell-Hearn (GDH) sum near the photon point.  
 264 The original GDH sum rule [31, 32], defined for real photons,  
 265 is a fundamental prediction on the nucleon's spin structure  
 266 that relates the helicity-dependent total photo-absorption cross  
 267 section to the nucleon anomalous magnetic moment. The defi-  
 268 nition of the GDH sum has been generalized to virtual pho-  
 269 tons [33, 34], and the value of the generalized GDH sum at  
 270 low  $Q^2$  has been predicted in the chiral perturbation theory.  
 271 Similar to the pion production results presented here, the goal  
 272 of the EG4's inclusive analysis is to test the chiral pertur-  
 273 bation theory prediction and to compare the extrapolation to the  
 274  $Q^2 = 0$  point with the GDH sum rule of the real photon.

275 The experiment was carried out in 2006 in experimental  
 276 Hall B of JLab. Inclusive data were collected in the range  
 277  $1 < W < 2 \text{ GeV}/c^2$  and  $Q^2$  down to 0.015  $(\text{GeV}/c)^2$  [35],  
 278 using six beam energies (1.1, 1.3, 1.5, 2.0, 2.3, 3.0 GeV) on  
 279 a polarized  $\text{NH}_3$  target and two energies (1.3, 2.0 GeV) on a  
 280 polarized  $\text{ND}_3$  target. The average polarizations of  $\text{NH}_3$  and  
 281  $\text{ND}_3$  typically ranged within (75–90)% and (30–45)%,  
 282 respectively. For the exclusive channel, only  $\text{NH}_3$  data with  
 283 beam energies of 1.1, 1.3, 2.0, 2.3, and 3.0 GeV were analyzed  
 284 with the lowest  $Q^2$  being 0.0065  $(\text{GeV}/c)^2$ . The 1.5 GeV en-  
 285 ergy data were excluded because they were taken for run com-  
 286 misioning purpose and had limited statistics. For  $\text{ND}_3$  data,  
 287 the target spin direction was not flipped during the run, which  
 288 makes it impossible to extract  $A_{UL}$  nor the complete informa-  
 289 tion on  $A_{LL}$  from the exclusive channel.

### A. The CLAS Detector

290 The CEBAF Large Acceptance Spectrometer (CLAS) was  
 291 used to detect scattered particles [36]. Figure 2 shows the ba-  
 292 sic structure of CLAS during EG4 with the polarized target  
 293 installed. CLAS is an almost hermetic detector, optimized for  
 294 the measurement of multi-particle final states in a large mo-  
 295 mentum region. The detector design is based on a toroidal  
 296 magnet made by six superconducting coils arranged around  
 297 the beam line to produce a field pointing primarily in the az-  
 298 imuthal direction. The field direction can be set such that

301 the scattered negatively-charged particles can be either bent  
 302 away from the beamline (“electron outbending”) or towards it  
 303 (“electron inbending”). The detector itself is composed of six  
 304 independent magnetic spectrometers, referred to as six “sec-  
 305 tors”, with a common target, trigger, and data acquisition sys-  
 306 tem. Each sector is equipped with a three-layer drift cham-  
 307 ber system (DC) for momentum and tracking determination, a  
 308 time-of- light (TOF) counter, a Cherenkov Counter (CC) and  
 309 a double-layer Electromagnetic Calorimeter (EC). The TOF,  
 310 CC and the EC systems are primarily used for determining  
 311 the particle type.

312 In order to reach very low  $Q^2$  while retaining the high beam  
 313 energy needed to measure the GDH sum, a small scattering  
 314 angle was necessary. This was achieved by running the CLAS  
 315 torus magnet in the electron-outbending con guration. Al-  
 316 though the standard CLAS Cherenkov detector geometrically  
 317 reaches an 8 scattering angle [37], its structure is not ideal  
 318 for collecting the Cherenkov light for outbending electrons.  
 319 Therefore, for the EG4 experiment, a new Cherenkov detector  
 320 was built by the INFN-Genova group and installed in sector 6,  
 321 as shown in Fig. 2. It was designed to reach 6 scattering angle  
 322 by optimizing the light collection for the electron-outbending  
 323 con guration. Due to the very high counting rates at such low  
 324 scattering angles, instrumenting only one CLAS sector was  
 325 suf cient for the experiment. The new Cherenkov detector  
 326 used the same radiator gas ( $C_4F_{10}$ ) and the gas ow control  
 327 system used in the standard CLAS Cherenkov. It consisted  
 328 of 11 segments, each equipped with a pair of light-weight  
 329 spherical mirrors, see Fig. 3. The mirrors were constructed  
 330 following [38], by shaping a plexiglass layer onto a spheri-  
 331 cal mould, then gluing onto it a sandwich of carbon ber and  
 332 honeycomb, and nally evaporating a thin layer of aluminum  
 333 onto the plexiglass. Each mirror re ected the light towards a  
 334 light collector made of two pieces, an entrance section with  
 335 the approximate shape of a truncated pyramid and a guiding  
 336 section cylindrical in shape such as to match the circular pho-  
 337 tocatode. Each light collector was made of plexiglass with  
 338 aluminum evaporated on the internal surface. The entrance  
 339 section was built by a no-contact technique, where the plex-  
 340 iglass sheet was heated and pushed against a mould with the  
 341 desired shape, then the bottom of the obtained object was cut  
 342 to permit the free passage of light. The cylindrical section was  
 343 obtained by cutting a plexiglass tube. The two sections were  
 344 then glued together before evaporating the re ective layer. For  
 345 the PMTs, the Photonis XP4508B with quartz window were  
 346 chosen. The photoelectron yield was greater than 10 within  
 347 the kinematic region of the experiment, thereby yielding a  
 348 high electron detection ef ciency down to a scattering angle  
 349 of about 6 . Signals from the new Cherenkov were built into  
 350 the main electron trigger during EG4. Consequently only 1/6  
 351 of the full azimuthal acceptance of CLAS was used to detect  
 352 and identify forward-angle scattered electrons.

354

## B. The Polarized Electron Beam

355 The polarized electron beam was produced by illuminating  
 356 a strained GaAs photocathode with circularly polarized light.

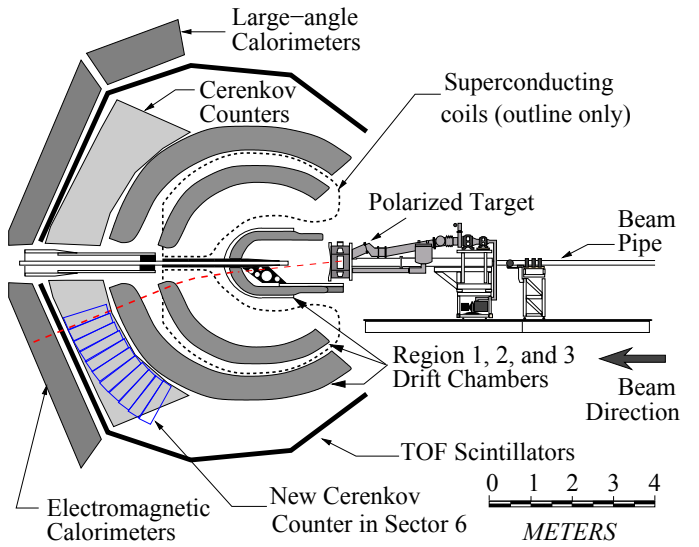


FIG. 2. (Color online) CLAS during EG4 showing the polarized target and the detector arrangement. A new Cherenkov detector consisting of 11 segments was installed in place of the original Cherenkov in sector 6. It provided the ability of detecting scattered electrons in the outbending con guration with scattering angles as small as 6 (dashed-line track).

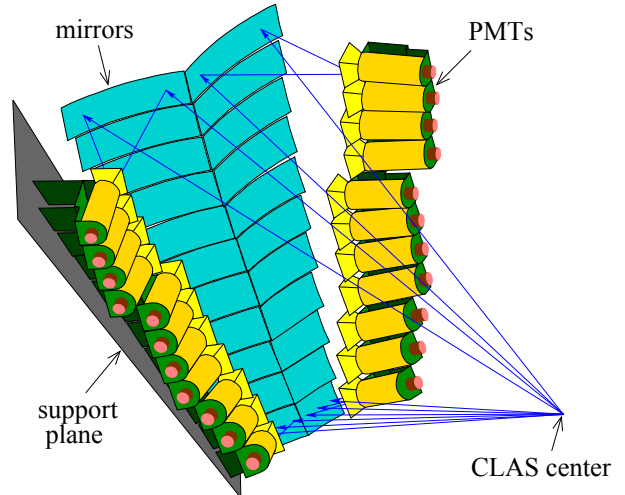


FIG. 3. (Color online) The new Cherenkov detector designed and built by the INFN-Genova group. It consists of 11 pairs of mirrors with spherical curvature, which re ect the Cherenkov light to corresponding photo-multiplier tubes (PMTs). Only one of the two support planes for the PMTs is shown here. The solid blue lines show simulated particle trajectories originated from the CLAS center and the re ection of the Cherenkov light towards the PMT.

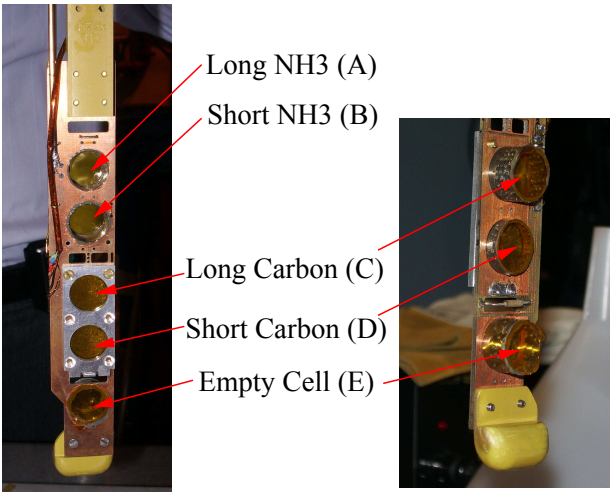
357 The helicity of the electron beam was selected from a pseudo-  
 358 random sequence, and followed a quartet structure of either  
 359 “+ +” or “ ++ ”, with each helicity state lasting 33 ms.  
 360 The helicity sequence controlled the trigger system, and peri-  
 361 ods of beam instability due to helicity reversal were rejected  
 362 from the data stream. To reduce possible systematic uncer-  
 363 tainties, data were taken for two different beam helicity con-

364 gurations, with the beam insertable half-wave plate (IHWP)  
 365 inserted (in) and removed (out), respectively. The polariza-  
 366 tion of the electron beam was measured by both a Møller and  
 367 a Mott polarimeter.

368

### C. The Polarized Targets

369 The polarized targets used for EG4 were the frozen  $^{15}\text{NH}_3$   
 370 and  $^{14}\text{ND}_3$  targets dynamically polarized at 1 K with a 5-  
 371 Teslaeld. These were the same as the targets used for pre-  
 372 vious CLAS double-polarization measurements [39]. The tar-  
 373 get material was irradiated with 20 MeV electrons prior to the  
 374 experiment to impart the paramagnetic radicals necessary for  
 375 dynamic polarization. It was subsequently stored in liquid ni-  
 376 trogen ( $\text{LN}_2$ ) until needed for the experiment. The material,  
 377 in the form of 1-2 mm sized granules, was then removed from  
 378 the  $\text{LN}_2$  storage dewars and loaded into two cylindrical con-  
 379 tainers on the target insert. The structure of the target insert is  
 380 shown in Fig. 4. The containers were either 1.0 cm or 0.5 cm  
 381 in length, hereafter referred to as the long and short cells, re-  
 382 spectively. The insert was then quickly placed into the target  
 383 “banjo”, a 1-2 liter vessel of 1-K liquid helium at the center of  
 384 a 5-T superconducting split coil magnet. A complete descrip-  
 385 tion of the polarized target can be found in Ref. [40].



386 FIG. 4. (Color online) Target insert used during the EG4 experiment.  
 387 A 1.0-cm long  $\text{NH}_3$  and the 0.5-cm long  $\text{NH}_3$  targets were installed  
 388 in the Long and Short  $\text{NH}_3$  positions during the first half of the  $\text{NH}_3$   
 389 run period. They were called the “long  $\text{NH}_3$  top” and the “short  
 390  $\text{NH}_3$ ” targets, respectively. During the second half of the  $\text{NH}_3$  run,  
 391 two 1.0-cm long  $\text{NH}_3$  targets were installed in the Long and the Short  
 392 positions; they were called the “long  $\text{NH}_3$  top” and the “long  $\text{NH}_3$   
 393 bottom” targets, respectively. For the  $\text{ND}_3$  run period only one 1.0-  
 394 cm long  $\text{ND}_3$  target was installed in the Short position. The five  
 395 target positions are labeled A, B, C, D, and E, as shown.

396

397 Due to the presence of gaps between the frozen crystals  
 398 inside the target cell, even if the length of the target cell or  
 399 the banjo could be determined precisely, the exact amount of  
 400 polarized materials interacting with the electron beam could

TABLE I. Targets used during EG4 along with their target lengths and densities. The target ID was the value recorded in the data. ID 10 was not used. The target position refers to the physical location on the target insert defined in Fig. 4.

Target ID	Target type	Target position	length (cm)	Density (g/cm <sup>3</sup> )
1	long $\text{NH}_3$ top	A	1.0	0.917 <sup>a</sup>
2	long $\text{ND}_3$	B	1.0	1.056 <sup>a</sup>
3	empty cell with helium	E	1.0	0.145 <sup>b</sup>
4	long carbon	C	1.0, 0.216 <sup>c</sup>	2.166 <sup>d</sup>
5	short $\text{NH}_3$	B	0.5	0.917 <sup>a</sup>
6	short carbon	D	0.5, 0.108 <sup>c</sup>	2.166 <sup>d</sup>
7	long carbon no helium	C	1.0, 0.216 <sup>c</sup>	2.166 <sup>d</sup>
8	empty cell without helium	E	1.0	
9	short carbon without helium	D	0.5	2.166 <sup>c</sup>
11	long $\text{NH}_3$ bottom	B	1.0	0.917 <sup>a</sup>

<sup>a</sup> For polarized  $\text{NH}_3$  or  $\text{ND}_3$  the densities are the density of the frozen polarized material beads.

<sup>b</sup> Helium density.

<sup>c</sup> The first and the second length values correspond to the cell length and the carbon foil thickness, respectively.

<sup>d</sup> Carbon density.

396 not be directly measured. The fraction of the target filled by  
 397 frozen polarized material is called the “packing factor” and is  
 398 typically extracted by comparing the yield from the polarized  
 399 target to those from carbon and “empty” targets. For the car-  
 400 bon target, a carbon foil with known thickness was placed in  
 401 an empty target cell and filled with liquid  $^4\text{He}$ . There were two  
 402 carbon targets, labeled “long” and “short” carbon, of which  
 403 both the cell length and the foil thickness match those of the  
 404 long and the short  $\text{NH}_3$  targets, respectively. Empty targets  
 405 refer to target cells with no solid material inside. Empty tar-  
 406 gets can either be filled with liquid  $^4\text{He}$ , or the  $^4\text{He}$  can be  
 407 completely pumped out. There was only one empty cell dur-  
 408 ing EG4 to physically host the empty targets, which was 1.0  
 409 cm in length.

410 During EG4 the polarized target was placed 1.01 m up-  
 411 stream from the CLAS center to increase the acceptance at  
 412 low  $Q^2$  by reducing the minimum angle for the scattered elec-  
 413 trons. The following targets were used: two 1.0-cm long and  
 414 one 0.5-cm long  $\text{NH}_3$  target, one 1.0-cm long  $\text{ND}_3$  target, one  
 415 0.216-cm and one 0.108-cm thick  $^{12}\text{C}$  target, and one empty  
 416 target. The target types during EG4 are defined in Table I. Un-  
 417 less specified otherwise, “empty target” refers to target type 3  
 418 [empty cell with helium (1 cm)] hereafter.

419 An NMR system was used to monitor the polarization of  
 420 the target during the experiment, but was subject to three sys-  
 421 tematic uncertainties that limited its suitability for data anal-  
 422 ysis. First, the NMR coils were wrapped around the outside  
 423 of the 1.5-cm diameter target cells, while the electron beam  
 424 was only rastered over the central 1.2 cm portion of the target.  
 425 The NMR signal was thus dominated by the material at the

edges of the cell, and lacked sensitivity to the beam-induced depolarization of the material at the center. This uncertainty is difficult to estimate, as the effect depends on the accumulated dose. Second, for the EG4 experiment the two polarized target cells were adjacent to one another on the insert, as shown in Fig. 4, and cross-talk was observed between the cells' NMR circuits. Tests performed at the end of the experiment indicate that cross-talk could contribute an uncertainty of about 5-10% to the polarization measurement due to its effect on the thermal-equilibrium calibration of the NMR signal. Third, calibration of the NMR system itself is normally subject to a 4-5% uncertainty. These three effects added up to a large systematic uncertainty to the target polarization measured by NMR. Therefore, it was decided that the asymmetries of  $ep$  elastic scattering would be used to extract the product of the beam and target polarizations  $P_b P_t$  needed for the exclusive channel analysis reported here. The methods and results for the elastic  $P_b P_t$  extraction will be described in Section III D. For  $\text{NH}_3$ , the use of  $^{15}\text{N}$  has the advantage that only one unpaired proton can be polarized, while all neutrons are paired to spin zero. The polarized proton in the  $^{15}\text{N}$  does however affect the measured asymmetry by a small amount, as discussed in Section III G.

### 446 III. DATA ANALYSIS

#### 447 A. Exclusive Event Selection

448 Exclusive events  $\vec{e}\vec{p} \rightarrow e'\pi^+(n)$  were identified by detecting the final state electron in coincidence with a pion and using a missing mass cut to select the undetected neutron. For each event, we required that two particles be detected with the correct charges (-1 for the electron and +1 for the  $\pi^+$ ). Each particle was required to have valid information from DC and TOF, and have reconstructed momentum greater than 0.3  $\text{GeV}/c$  (0.1  $\text{GeV}/c$  higher than the momentum acceptance of CLAS [36]).

457 For particle identification, EC and CC signals were used 458 to identify electrons. Cuts were applied on the EC:  $E_{tot} > 459 (p - 0.3) \times 0.22$ ,  $E_{in} > (0.14p - 0.8E_{out})$  and  $E_{in} > 0.035p$ , 460 where  $E_{in}$  and  $E_{out}$  are the energy deposited in the inner and 461 the outer layers of the EC, respectively;  $E_{tot} = E_{in} + E_{out}$  462 and  $p$  is the particle momentum in  $\text{GeV}/c$ . These cuts were 463 selected to optimize the separation of electrons (that produce 464 electromagnetic showers) from pions (that deposit energy mostly 465 through ionizations). We also required there to be only one hit in the CC, with its signal consistent with those 466 from the EC and the TOF in both hit position and timing.

468 Pions were determined from a mass cut of  $0.01 < m < 469 0.30 \text{ GeV}/c^2$  and a TOF cut  $|t_{TOF} - t_{\text{expected}}^\pi| < 1.0 \text{ ns}$ . 470 The expected flight time of the pion,  $t_{\text{expected}}^\pi$ , was calculated 471 from the particle's momentum in combination with the timing 472 of the electron. Figure 5 shows the effect of the TOF cut on 473 the  $\beta \equiv v/c$  vs. momentum  $p$  distributions, where  $v$  is the 474 velocity amplitude (speed) of the particle. The TOF cut used 475 clearly selected pions out of other particle background.

476 For each event, a vertex  $z$  was used. Here  $z$  is defined as

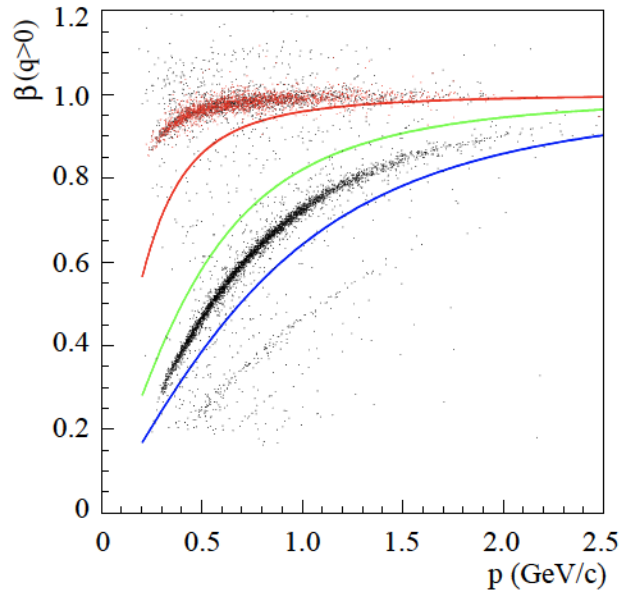


FIG. 5.  $\beta$  vs.  $p$  for all positively charged particles, with (red) and without (black) TOF cut for pions. The red, green and blue curves correspond to reconstructed masses of 0.3, 0.7 and  $1.2 \text{ GeV}/c^2$ , respectively, which are typical cut-off values used to distinguish between pions and kaons, kaons and protons, and protons and heavier particles. As can be seen, the positively charged particles detected consist of significant fractions of protons and heavier particles and a small fraction of kaons, but the  $\pm 1.0 \text{ ns}$  TOF cut is quite effective in selecting pions. These data were collected on the long top  $\text{NH}_3$  target during the 3 GeV run period.

477 pointing along the beam direction with the origin coincides 478 with the CLAS center. The polarized target was positioned 479 upstream of the CLAS center during EG4 (see Fig. 2), and the 480 center of the target was determined from empty target data to 481 be at  $z = -101 \text{ cm}$ . The  $z$  cut was optimized to be

$$482 -106 \text{ cm} < z < -96 \text{ cm} , \quad (22)$$

483 where the range was determined using empty target data to 484 exclude as much material outside the target as possible. See 485 Fig. 7 in Section III C for a detailed presentation of the vertex 486  $z$  distribution.

487 Acceptance cuts, also called “fiducial cuts”, were applied 488 on both electrons and pions using reconstructed DC variables. 489 These acceptance cuts exclude regions where the detector ef- 490 ficiency is not well understood, which often happens on the 491 edge of the detectors, but could also include regions where 492 certain parts of the detectors malfunctioned. Moreover, be- 493 cause the main purpose of EG4 was measurement of the GDH 494 sum, which only requires detection of inclusively-scattered 495 electrons, not all six DC sectors were turned on during the 496 run. This caused a variation in the  $\phi^*$  acceptance of the exclu- 497 sive channel. Determination of the acceptance and its effects 498 on the asymmetries will be described in Sec. III H.

499

## B. Beam Properties

500 As described in the previous section, the helicity of the electron beam followed a quartet structure. For EG4, the beam 501 helicity of each event was delayed by 8 pulses (2 quartets) 502 and then recorded in the data stream. This delayed recording 503 helped to avoid cross-talk between the helicity signal and the 504 electronics or data acquisition system in the hall. In the data 505 analysis, the delay of the helicity sequence was corrected to 506 match each event to its true beam helicity state. During this 507 process, events with inconsistent recording of the helicity sequence 508 were rejected.

510 A helicity dependence of the integrated beam charge causes 511 a first-order correction to the measured physics asymmetry, 512 and thus it is desired to keep the charge asymmetry as small 513 as possible. The beam charge asymmetry was calculated using 514 the charge measured by the Faraday cup. It was found to be 515 below the percent level throughout the EG4 experiment, and 516 for most runs had stable values at or below the  $10^{-3}$  level.

517 Different methods for deriving the beam energy were used 518 during EG4. The exact energies were 1.054, 1.338, 1.989, 519 2.260 and 2.999 GeV. The beam polarization was determined 520 using a Møller polarimeter [36] in Hall B that measured the 521 asymmetry in elastic electron-electron scattering. The re- 522 sults are shown in Fig. 6. Typically, Møller measurements 523 were performed as soon as a change to the beam configu- 524 ration was made, and then intermittently throughout the run 525 period. Therefore, the beam polarization from each Møller 526 measurement was applied retroactively to runs that immedi- 527 ately follow such configuration changes, and to runs that fol- 528 low the Møller measurement until the next valid measure- 529 ment is available. Two additional measurements were done 530 using a Mott polarimeter [41–44], which is located near the 531 injector where the beam electrons have reached 5 MeV in en- 532 ergy but before entering the first linac. The Mott polarime- 533 ter results were consistent with those from Møller measure- 534 ments. The absolute beam helicity was determined using the 535  $\sin^{-1}$ -weighted moment of the beam asymmetry  $A_{LU}$  in the 536 (1232)3 2<sup>+</sup> region and comparing with results from previ- 537 ous experiments [45, 46]. Using the  $A_{LU}$  method, it was de- 538 termined that when the beam IHWP is inserted, for beam ener- 539 gies 1.3 and 2.3 GeV, the positive DAQ helicity corresponds to 540 the true negative helicity of the beam electron, while for other 541 energies the positive DAQ helicity corresponds to the true posi- 542 tive electron helicity. These results are consistent with the sign 543 change of the beam polarization measured with the Møller po- 544 larimeter.

545

## C. Kinematic Corrections

546 Various corrections were applied to the kinematic variables 547 reconstructed from the detectors [47]. The first is the raster 548 correction: in order to avoid the electron beam overheating the 549 target, the beam was rastered in a circular pattern during EG4 550 using four magnets located upstream of the target. The values 551 of the magnet current were recorded in the data stream and 552 were used to calculate the beam position ( $x$   $y$ ) at the target.

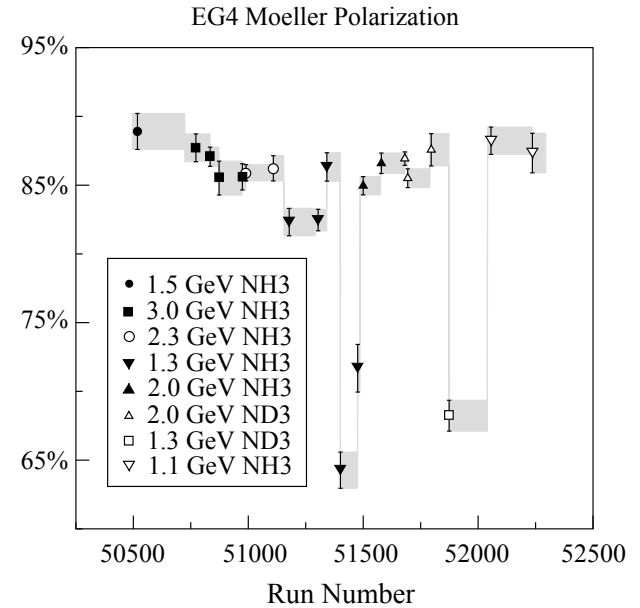


FIG. 6. Beam polarization from Møller measurements vs. run number for the whole EG4 experiment. The grey bands represent extrapolations of the beam polarization to the corresponding range of runs as described in the text.

553 The beam position was then used to re-calculate the vertex po- 554 sition along the beam direction  $z$ . After the raster correction 555 was applied, the average value of the  $z$  positions of all parti- 556 cles in the same event was taken as the true vertex position of 557 the event, see Fig. 7 [47]. The polar and the azimuthal angles 558 and of each particle were also corrected using the new 559 beam and vertex positions. This procedure took into account 560 the multiple scattering effect that affected the reconstructed 561 vertex position randomly for each particle.

562 Due to uncertainties in our knowledge of the drift chamber 563 positions and of the shape and location of the torus coils, a 564 systematic shift of the particle momentum was present. To 565 correct for this shift, the magnitude of the reconstructed par- 566 ticle momentum  $p$  and the polar angle were adjusted us- 567 ing sector-dependent parameters. The detailed method for the 568 momentum correction is described in Ref. [48] and results for 569 this experiment are given in Ref. [47]. For sector 6 equipped 570 with the new Cherenkov counter, inclusive elastic  $ep$  scatter- 571 ing events were used to optimize the correction based on the 572 invariant mass  $W$  position of the elastic peak. For the other 573 sectors, electron triggers were not available and hadrons from 574 exclusive events such as  $ep \rightarrow e p X$ ,  $ep \rightarrow e^+ p^- X$ , and 575 exclusive events  $ep \rightarrow e p^+ p^-$  were used to optimize the 576 corrections.

577 Finally, the momentum of each particle was corrected for 578 the energy loss due to passage through material enclosed in 579 the target banjo and the target windows. For electrons a single 580 value  $dE/dx = 2.8 \text{ MeV}/(\text{g}/\text{cm}^2)$  was used, while for other 581 particles the Bethe-Bloch equation [49] was used to calculate 582 the ionization loss.

583 Figure 8 shows the effect on the missing mass spectrum for

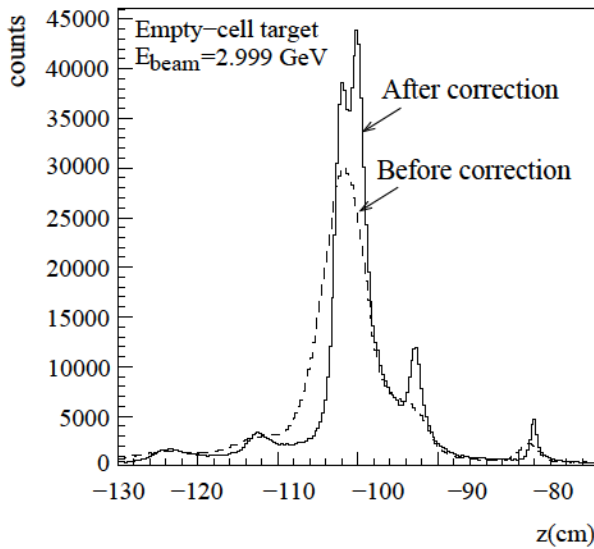


FIG. 7. Electrons' vertex  $z$  position before (dashed) and after (solid) raster corrections, taken with the empty target with the 3 GeV beam. While the beam line exit window (at  $z = -78.3$  cm) can be seen both before and after the correction, the banjo windows (at  $z = -100$  and  $-102$  cm), the 4 K heat shield (14  $\mu\text{m}$  aluminum at  $z = -121.0$  cm), some target structure at  $z \approx -112$  cm, and several insulating foils (aluminum or aluminized mylar, between  $z = -90.5$  and  $-94.1$  cm), become visible only after the raster correction. The vertex  $z$  cut, Eq. (22), corresponds to slightly more than  $3\sigma$  in the target thickness [47].

the  $ep \rightarrow e'\pi^+(X)$  channel from kinematic corrections.

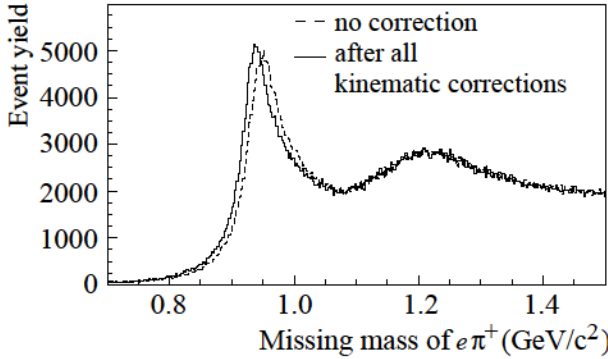


FIG. 8. Missing mass spectrum for the  $e + p \rightarrow e'\pi^+(X)$  channel before (dashed) and after all kinematics corrections (solid), from six 3.0-GeV long top  $\text{NH}_3$  target runs. After all corrections, the peak center is closer to the expected value (the neutron mass).

585  
586

#### D. Elastic Scattering for Extracting $P_bP_t$

588 The product of the beam and the target polarizations  $P_bP_t$  is needed to directly correct the exclusive channel asymmetries. During EG4, the target polarization  $P_t$  was measured by

591 NMR and the beam polarization  $P_b$  by the Møller polarimetry. 592 However, due to reasons described in Section II C, the NMR 593 measurements had large uncertainties and an alternate method 594 had to be used. For EG4 we extracted  $P_bP_t$  for all beam en- 595 ergies by comparing the double spin asymmetry of elastic  $ep$  596 events to the expected value:

$$597 \quad P_bP_t = \frac{A_{\text{meas}}^{\text{el}}}{A_{\text{th}}^{\text{el}}}, \quad (23)$$

598 where the measured elastic asymmetry was extracted from 599 data using

$$600 \quad A_{\text{meas}}^{\text{el}} = \frac{A_{\text{raw}}^{\text{el}}}{f_{\text{el}}}, \quad (24)$$

601 with  $f_{\text{el}}$  the elastic dilution factor to account for the effect of 602 events scattered from unpolarized material in the target. The 603 raw asymmetry was evaluated as

$$604 \quad A_{\text{raw}}^{\text{el}} = \frac{\frac{N_{R(L)}^{\text{el}}}{Q_R} - \frac{N_L^{\text{el}}}{Q_L}}{\frac{N_R^{\text{el}}}{Q_R} + \frac{N_L^{\text{el}}}{Q_L}}, \quad (25)$$

605 where  $N_{R(L)}^{\text{el}}$  and  $Q_{R(L)}$  are the elastic event yield and the 606 beam charge for the right- (left-)handed beam electrons, re- 607 spectively. The expected elastic-scattering asymmetry  $A_{\text{th}}^{\text{el}}$  608 was calculated using

$$609 \quad A_{\text{th}}^{\text{el}} = -2\sqrt{\frac{\tau}{1+\tau}} \tan \frac{\theta_e}{2} \\ 610 \quad \times \frac{\left[ \sqrt{\tau(1+(1+\tau)\tan^2 \frac{\theta_e}{2})} \cos \theta_e + \sin \theta_e \frac{G_E^p}{G_M^p} \right]}{\left[ \frac{(G_E^p/G_M^p)^2 + \tau}{1+\tau} + 2\tau \tan^2 \frac{\theta_e}{2} \right]} \quad (26)$$

611 with  $\tau = Q^2/(4M^2)$ . The proton form factor fits from 612 Ref. [50] were used:

$$613 \quad G_E^p = 1/[1 + 0.62Q + 0.68Q^2 + 2.8Q^3 + 0.83Q^4] \quad (27)$$

614 and

$$615 \quad G_M^p = 2.79/[1 + 0.35Q + 2.44Q^2 \\ 616 \quad + 0.5Q^3 + 1.04Q^4 + 0.34Q^5] \quad (28)$$

617 with  $Q \equiv \sqrt{Q^2}$  in  $\text{GeV}/c$ . Using a more updated fit of the 618 proton form factors than Ref. [50] would change the asymme- 619 try value by less than 2% relative.

620 Elastic events were identified using two methods: 1) in- 621 clusive elastic events where only the scattered electron was 622 detected and a cut on the invariant mass  $W$  near the pro- 623 ton peak was applied; and 2) exclusive elastic events where 624 both the scattered proton and electron were detected and cuts 625 were applied to the electron and the proton azimuthal angles: 626  $|\phi_e - \phi_p - 180^\circ| < 3^\circ$ , the polar angles of the proton and 627 the electron's momentum transfer  $\vec{q}$ :  $|\theta_p - \theta_q| < 2^\circ$ , and the 628 missing energy  $E_{\text{miss}} < 0.15$  GeV. The exclusive analysis 629 had limited statistics and only worked for the 3.0 and the 2.3 630 GeV data sets. For lower beam energies, the proton's scatter- 631 ing angle was typically greater than  $49^\circ$ , and was blocked by

the polarized target coils. Therefore the  $P_b P_t$  value extracted from exclusive elastic events was only used as a cross-check of the  $P_b P_t$  from inclusive events.

The presence of unpolarized material reduces the measured asymmetry, and this effect is described as a dilution factor in the analysis. The dilution factor for the inclusive elastic events,  $f_{el}^{incl}$ , was extracted by comparing the invariant mass  $W$  spectrum of the polarized target to that computed for the unpolarized material. The beam-charge-normalized  $W$  spectrum for the unpolarized material in the polarized target, denoted as  $\frac{N_{N \text{ in } NH_3}}{Q_{NH_3}}$ , was calculated using the spectra of the carbon and the empty target, the known thickness and density of the carbon and the empty target, and the polarized target's packing factor  $x_{NH_3}$  defined as the absolute length of the polarized material in the polarized target:

$$r_C = \frac{N_{N \text{ in } NH_3}}{Q_{NH_3}} = r_C \frac{N_{^{12}C}}{Q_{^{12}C}} + r_{\text{empt}} \frac{N_{\text{empt}}}{Q_{\text{empt}}} \quad (29)$$

where  $N_{^{12}C(\text{empt})}$  and  $Q_{^{12}C(\text{empt})}$  are the yield and the beam charge of the carbon (empty) target data. The scaling factors are

$$r_C = \frac{B_{NH_3} \cdot NH_3 x_{NH_3} + B_w \cdot w x_w \frac{x_{NH_3}}{l}}{B_{^{12}C} \cdot ^{12}C x_{^{12}C} + B_w \cdot w x_w \frac{x_{^{12}C}}{l}} \quad (30)$$

$$r_{\text{empt}} = 1 - \frac{x_{NH_3}}{l} - 1 - \frac{x_{^{12}C}}{l} \quad r_C \quad (31)$$

where  $x_{^{12}C}$  is the thickness of the carbon foil in the carbon target,  $x_w$  is the sum of thicknesses of other unpolarized material in the target,  $l$  is the target banjo length (1.0 cm for the long target and 0.5 cm for the short target), and  $B_{^{12}C} w = 1$  are the bound-nucleon fractions of the carbon target and other unpolarized material in the target, respectively. The values of  $x$  for the various materials are given in Table II. The bound-nucleon fraction for the  $NH_3$  target takes into account both the fraction of bound nucleons and a correction for the extra neutron in the  $^{15}N$ :  $B_{NH_3} = (14 + n_N) / 18$  with  $n_N = (p + n) / 2$  and  $p, n$  are the calculated elastic cross sections for the proton and the neutron, respectively.

After the contribution from the unpolarized material was known, the dilution factor was calculated using

$$f_{el}^{incl} = \frac{N_{p \text{ in } NH_3}}{N_{NH_3}} = \frac{N_{NH_3}}{N_{NH_3}} \frac{N_{N \text{ in } NH_3}}{N_{NH_3}} \quad (32)$$

where  $N_{NH_3}$  is the total number of events from the  $NH_3$  target. The dilution correction to the elastic asymmetry was then applied using Eq. (24). In the present analysis, elastic events below  $Q^2 = 0.156$  ( $GeV/c^2$ ) could not be used because of electrons scattered elastically from nuclei in the target, such as  $^{4}He$  and nitrogen. These low  $Q^2$  bins were rejected in the  $P_b P_t$  analysis.

Figure 9 shows the  $W$  spectrum decomposition for 1.1 and 3.0  $GeV$  inclusive elastic scattering data for two  $Q^2$  bins. The low  $Q^2$  bin (top) is to illustrate the effect of the nuclear elastic scattering and these bins were rejected from the  $P_b P_t$  analysis. The high  $Q^2$  bin (bottom) shows no such effect and the  $P_b P_t$  extracted are considered reliable. After the  $P_b P_t$  value was extracted for individual  $Q^2$  bins, the results were checked to

TABLE II. Material used for the EG4 target and their locations in increasing order of  $z$ , in the range  $z = (-120 \text{ to } 80) \text{ cm}$ . The ratios  $Z/A$  were used in the dilution factor analysis of the exclusive channel, see Sec.III F.

location $z$ (cm)	Material	Density ( $\text{g/cm}^3$ )	Thickness	$Z/A$
-101.9	banjo entrance window, Al	2.7	71 m	13 26 982
varies	target entrance window, kapton	1.42	25 m	0.51264
varies	$NH_3$	0.917	$x^a$	7 18
varies	long $^{12}C$	2.166	2.16 0.05 mm	6 12
varies	liquid $^4He$	0.145	$l \cdot x^a$	2 4
varies	target entrance window kapton	1.42	25 m	0.51264
-99.6	banjo exit window Al	2.7	71 m	13 26 982

<sup>a</sup>  $l$  is the banjo length and  $x$  is either the packing factor (for  $NH_3$  targets) or the carbon foil thickness (for carbon targets).

ensure there was no systematic  $Q^2$ -dependence, which would imply a problem with the analysis. The  $P_b P_t$  results were then averaged over all  $Q^2$  bins above 0.156 ( $GeV/c^2$ ). This was done for each individual run and the run-by-run,  $Q^2$ -averaged  $P_b P_t$  results were used to correct the asymmetries from the exclusive channel. Figure 10 illustrates the variation of  $P_b P_t$  during the experiment.

The uncertainty of the packing factor  $x_{NH_3}$  used in the analysis was checked using the  $W$  spectrum below  $W = 0.9$  ( $GeV/c^2$ ), since an incorrect normalization would yield an over- or an under-subtraction of the yield from unpolarized material. For the 2.3 and 3.0  $GeV$  data the value of  $x_{NH_3}$  was confirmed by comparing the  $P_b P_t$  value extracted from the inclusive to that from the exclusive elastic events. The packing factor and its uncertainty also affect the dilution analysis of the exclusive channel, to be described in the next sections, thus the final results on  $P_b P_t$  for each combination of beam energy and polarized target type are shown together with the exclusive channel dilution results in Table III. The relatively larger error bar for the 1.1  $GeV$   $NH_3$  long bottom target is because most of the data were affected by the nuclear elastic scattering and there are very limited  $Q^2$  bins available for the elastic  $P_b P_t$  analysis.

In addition to checking the  $W$  spectrum and the comparison between inclusive and exclusive elastic events, the  $e^- e^- (p)$  channel was also used to check  $x_{NH_3}$  because these events come primarily from the unpolarized neutrons of the nitrogen in the target and thus should have a dilution factor of zero. The  $e^- (p)$  events were analyzed for all beam energies and it was found the dilution factors calculated using the  $x_{NH_3}$  values in Table III were indeed consistent with zero. As a last check, the run-by-run values of  $P_b P_t$  were compared with the numerous target material and configuration changes during the experiment, and were found to be consistent with the physical changes of the target.

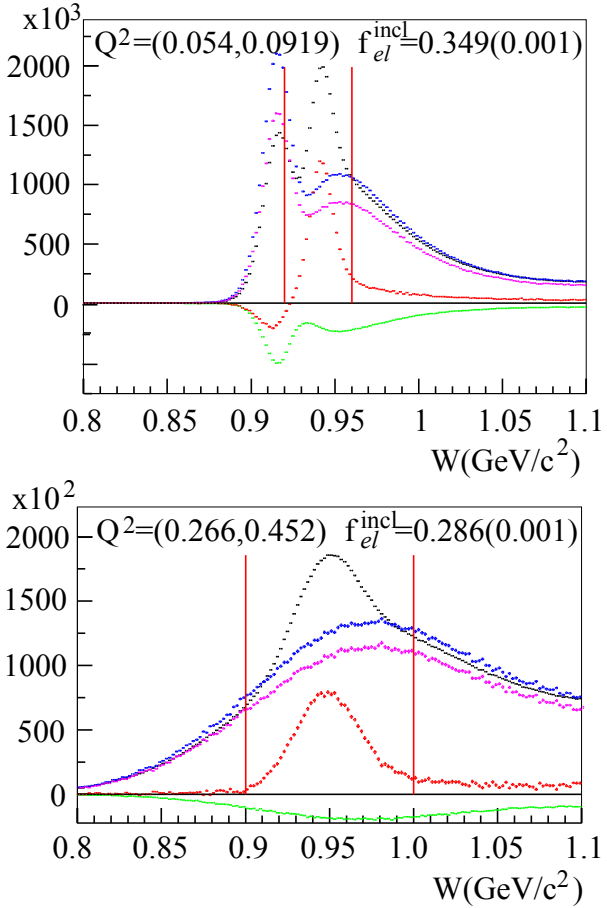


FIG. 9.  $W$ -spectrum for dilution calculation for inclusive elastic  $P_b P_t$  analysis. Top: 1.1 GeV data on  $\text{NH}_3$  long bottom target in the  $Q^2 = (0.054, 0.0919)$   $(\text{GeV}/c)^2$  bin; bottom: 3.0 GeV data on  $\text{NH}_3$  long top target in the  $Q^2 = (0.266, 0.452)$   $(\text{GeV}/c)^2$  bin. For each panel, histograms from the carbon target (blue) and empty target (green) were scaled using Eqs. (30-31) using a packing factor of 0.75 cm for 1.1 GeV and 0.65 cm for 3.0 GeV respectively, and their sum gave the estimated contribution from unpolarized material in the  $\text{NH}_3$  target (magenta). This unpolarized background was then subtracted from the  $\text{NH}_3$  spectrum (black) to estimate the contribution from polarized protons in the target (red). The calculated elastic dilution factors are shown for each set of data with their uncertainties in the brackets. The  $W$  cuts used to select elastic events are shown as the two red vertical lines. Note that the scaled empty target spectrum (green) is negative, indicating that for the chosen packing factor we have scaled up the carbon data and then subtracted the extra helium to reproduce the unpolarized background in  $\text{NH}_3$ . For  $Q^2$  bins below 0.156  $(\text{GeV}/c)^2$ , the nuclear elastic event contaminates the  $ep$  elastic peak and the extraction of the dilution factor is not reliable. For this reason, data with  $Q^2 < 0.156$   $(\text{GeV}/c)^2$  were rejected from the elastic  $P_b P_t$  analysis.

### E. Extraction of Exclusive Channel Asymmetries

To extract the exclusive channel asymmetries, the  $e^- + (n)$  channel events were divided into four-dimensional bins in  $W$ ,  $Q^2$ ,  $\cos\theta$  and  $\phi$  and then the asymmetries were extracted from the counts in each bin. The event counts for the four

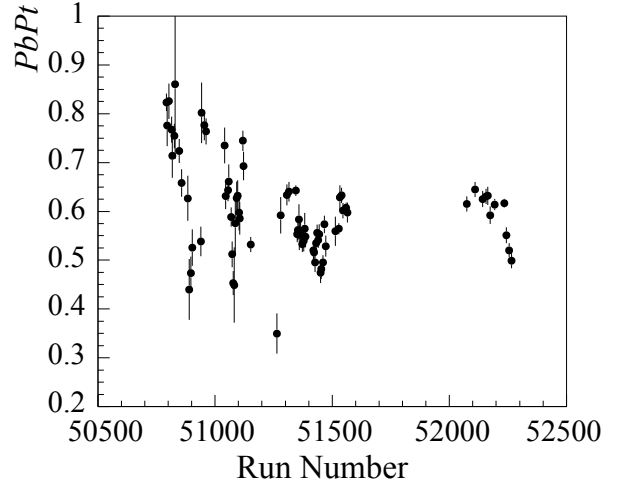


FIG. 10. Magnitude of  $P_b P_t$  extracted from inclusive elastic scattering events for all runs used in the present analysis that were taken on the polarized  $\text{NH}_3$  target. For illustration purposes, results from adjacent runs that shared the same beam insertable half-wave plate status were combined and are shown as one data point here. The error bars shown are statistical uncertainties determined by the number of available elastic events.

combinations of beam helicities and target polarization can be written, based on Eq. (5), as

$$724 \quad N = D_1 \quad 0 + P_b \quad e + f_{\text{dil}} P_t \quad t + P_b \quad f_{\text{dil}} P_t \quad et \quad (33)$$

$$725 \quad N = D_2 \quad 0 \quad P_b \quad e + f_{\text{dil}} P_t \quad t \quad P_b \quad f_{\text{dil}} P_t \quad et \quad (34)$$

$$726 \quad N = D_3 \quad 0 + P_b \quad e \quad f_{\text{dil}} P_t \quad t \quad P_b \quad f_{\text{dil}} P_t \quad et \quad (35)$$

$$727 \quad N = D_4 \quad 0 \quad P_b \quad e \quad f_{\text{dil}} P_t \quad t + P_b \quad f_{\text{dil}} P_t \quad et \quad (36)$$

728 where the arrows in the subscripts of  $N$  are for the beam helicities ( or ) and the target spin directions ( or ), respectively, with and being positive helicity or parallel to the 729 beam direction and and being negative helicity or anti- 730 parallel to the beam direction. The parameters  $P$  and  $P$  are 731 the statistically-averaged target or beam polarizations when 732 the target spin is aligned and anti-aligned to the beamline, re- 733 spectively. The dilution factor  $f_{\text{dil}}$  for the exclusive channel 734  $ep \rightarrow e^+ + (n)$  is defined as the fractional yield from the po- 735 larized proton in the  $\text{NH}_3$  target, which effectively changes 736 the target polarization. The four parameters  $D_{1,2,3,4}$ , relating 737 event counts to cross sections, are related to the total beam 738 charge, target thickness, spectrometer acceptance, and detec- 739 tor efficiencies for each configuration. For stable running pe- 740 riods with no significant change in the target cell, the spec- 741 trometer setting and the detector status, the  $D$  factor is strictly 742 proportional to the accumulated beam charge in each setting. 743 From Eqs. (33-36), one can form the asymmetries as:

$$746 \quad A_{LU} = \frac{1}{P_b \quad P_t}$$

$$747 \quad \left[ \frac{\left( \frac{N_{\uparrow\downarrow}}{D_3} - \frac{N_{\downarrow\uparrow}}{D_4} \right) P_b^{\uparrow\uparrow} P_t^{\uparrow\uparrow} + \left( \frac{N_{\uparrow\uparrow}}{D_1} - \frac{N_{\downarrow\downarrow}}{D_2} \right) P_b^{\uparrow\downarrow} P_t^{\uparrow\downarrow}}{\left( \frac{N_{\uparrow\uparrow}}{D_1} + \frac{N_{\downarrow\downarrow}}{D_2} \right) P_t^{\uparrow\downarrow} + \left( \frac{N_{\uparrow\downarrow}}{D_3} + \frac{N_{\downarrow\uparrow}}{D_4} \right) P_t^{\uparrow\uparrow}} \right], \quad (37)$$

$$748 \quad A_{UL} = \frac{1}{f_{\text{dil}}^{\pi}} \frac{\left( \frac{N_{\uparrow\uparrow}}{D_1} + \frac{N_{\downarrow\downarrow}}{D_2} \right) - \left( \frac{N_{\uparrow\downarrow}}{D_3} + \frac{N_{\downarrow\uparrow}}{D_4} \right)}{\left( \frac{N_{\uparrow\uparrow}}{D_1} + \frac{N_{\downarrow\downarrow}}{D_2} \right) P_t^{\uparrow\downarrow} + \left( \frac{N_{\uparrow\downarrow}}{D_3} + \frac{N_{\downarrow\uparrow}}{D_4} \right) P_t^{\uparrow\uparrow}} \quad (38)$$

$$749 \quad A_{LL} = \frac{1}{P_b^{\uparrow\uparrow} P_b^{\uparrow\downarrow} f_{\text{dil}}^{\pi}} \times \\ 750 \quad \left[ \frac{\left( \frac{N_{\uparrow\downarrow}}{D_3} - \frac{N_{\downarrow\uparrow}}{D_4} \right) P_b^{\uparrow\uparrow} - \left( \frac{N_{\uparrow\uparrow}}{D_1} - \frac{N_{\downarrow\downarrow}}{D_2} \right) P_b^{\uparrow\downarrow}}{\left( \frac{N_{\uparrow\uparrow}}{D_1} + \frac{N_{\downarrow\downarrow}}{D_2} \right) P_t^{\uparrow\downarrow} + \left( \frac{N_{\uparrow\downarrow}}{D_3} + \frac{N_{\downarrow\uparrow}}{D_4} \right) P_t^{\uparrow\uparrow}} \right]. \quad (39)$$

### F. Dilution Factor for the Exclusive Channel

752 In contrast to the dilution for inclusive  $P_b P_t$  analysis that  
753 has only  $Q^2$  dependence (Section III D), the dilution for ex-  
754 clusive pion production could vary with all four kinematic  
755 variables  $W$ ,  $Q^2$ ,  $\cos \theta^*$  and  $\phi^*$  [51]. To evaluate the dilu-  
756 tion factor for all 4-dimensional bins of  $(W, Q^2, \cos \theta^*, \phi^*)$ ,  
757 the yield from the unpolarized material inside the polarized  
758 NH<sub>3</sub> target was constructed using the missing mass spectra  
759 from the carbon and the empty targets. Scaling factors for  
760 the carbon and empty target data were calculated following  
761 a prescription similar to Eqs. (29-31), but with the bound-  
762 nucleon fraction  $B$  replaced by the ratio  $Z/A$  (Table II) for  
763 the  $ep \rightarrow e'\pi^+(n)$  [(1 -  $Z/A$ ) for the  $en \rightarrow e'\pi^-(p)$ ] chan-  
764 nel. For NH<sub>3</sub> one should use  $\frac{Z_{\text{NH}_3}}{A_{\text{NH}_3}} = 7/18$  to account for  
765 only unpolarized protons. We obtain:

$$766 \quad \frac{N_{\text{N in NH}_3}}{Q_{\text{NH}_3}} = a \left( \frac{N_{^{12}\text{C}}}{Q_{^{12}\text{C}}} \right) + b \left( \frac{N_{\text{empt}}}{Q_{\text{empt}}} \right), \quad (40)$$

767 where

$$768 \quad a = \frac{\left( \frac{Z_{\text{NH}_3}}{A_{\text{NH}_3}} \rho_{\text{NH}_3} x_{\text{NH}_3} \right) + \left( \frac{Z_w}{A_w} \rho_w x_w \right) \frac{x_{\text{NH}_3}}{l}}{\left( \frac{Z_{^{12}\text{C}}}{A_{^{12}\text{C}}} \rho_{^{12}\text{C}} x_{^{12}\text{C}} \right) + \left( \frac{Z_w}{A_w} \rho_w x_w \right) \frac{x_{^{12}\text{C}}}{l}}, \quad (41)$$

$$769 \quad b = \left( 1 - \frac{x_{\text{NH}_3}}{l} \right) - \left( 1 - \frac{x_{^{12}\text{C}}}{l} \right) a. \quad (42)$$

770 Similar to elastic analysis, the value of  $b$  from Eq. (42) could  
771 be either positive or negative depending on the input packing  
772 factor. Figure 11 shows the dilution factor evaluation for the  
773 3.0 GeV data using the NH<sub>3</sub> long top target.

774 From Eqs. (38-39) one can see that the uncertainties in  $P_b P_t$   
775 and  $f_{\text{dil}}^{\pi}$  should be evaluated at the same time because both  
776 depend on the packing factor. Table III shows all  $P_b P_t$  and  
777 dilution results for the packing factor range used in the elastic  
778  $P_b P_t$  analysis. For each setting of beam energy and target, we  
779 varied the packing factor by one standard deviation and eval-  
780 uated  $P_b P_t$  and  $f_{\text{dil}}^{\pi}$ . We used the observed difference in the  
781 product  $P_b P_t f_{\text{dil}}^{\pi}$  as the uncertainty due to the packing fac-  
782 tor, labeled as  $P_b P_t f_{\text{dil}}^{\pi} \pm (p.f.)$ . For the total uncertainty  
783  $\frac{\Delta(P_b P_t f_{\text{dil}}^{\pi})}{P_b P_t f_{\text{dil}}^{\pi}}$  (total), we added the following terms in quadra-  
784 ture: 1) statistical uncertainty of inclusive elastic events used  
785 in the  $P_b P_t$  analysis; 2) statistical uncertainty of the carbon  
786 and empty target counts used to calculate the dilution factor  
787 for inclusive elastic events; 3) statistical uncertainty in the ex-  
788 clusive  $ep \rightarrow e'\pi^+(n)$  channel due to limited statistics of car-  
789 bon and empty target data  $f_{\text{dil}}^{\pi} \pm (\text{stat.})$ ; and 4) the observed  
790 variation in  $P_b P_t f_{\text{dil}}^{\pi}$  when the input packing factor was var-  
791 ied within its uncertainty. The resulting total uncertainties on  
792  $P_b P_t f_{\text{dil}}^{\pi}$  were used for the evaluation of the uncertainty of  
793 the double-spin asymmetry  $A_{LL}$ . For the target asymmetry

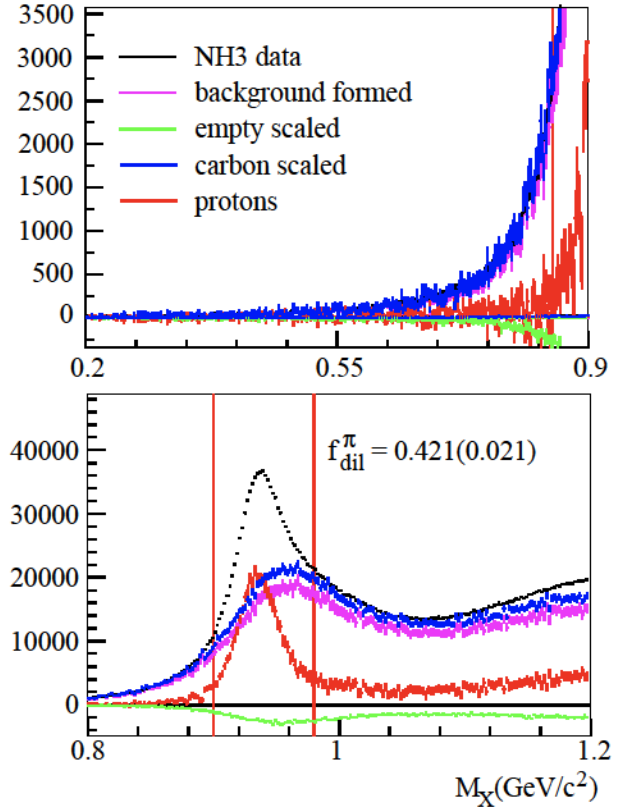


FIG. 11. Missing mass  $M_X$  spectrum for deriving the dilution factor for the  $ep \rightarrow e'\pi^+(n)$  channel. Top: missing mass below the neutron mass peak; bottom: missing mass around the neutron mass peak. The data shown are for the 3.0 GeV run period using the NH<sub>3</sub> long top target. Here, the  $M_X$  spectrum for the nuclear material (magenta) in the polarized NH<sub>3</sub> target was constructed using the spectra for the carbon target (blue), the empty target (green), with an input packing factor  $x = 0.65$  cm. The nuclear contribution was then subtracted from the NH<sub>3</sub> target spectrum (black) to give the polarized-proton spectrum (red). The dilution factor was evaluated using the region around the neutron peak and is shown in the bottom plot with the uncertainty in the bracket. The histogram and the dilution uncertainties include both statistical uncertainties and the uncertainty in the scaling or packing factors. Note that the empty target (green) spectrum is negative, indicating we have scaled up the carbon data and then subtracted the extra helium (empty target) to reproduce the unpolarized background in NH<sub>3</sub>. Results for the dilution factor is shown in the bottom plot. The  $M_X$  cuts (0.90, 0.98)  $\text{GeV}/c^2$  used in the dilution and the asymmetry analysis are shown by the two red vertical lines.

786 in the  $P_b P_t$  analysis; 2) statistical uncertainty of the carbon  
787 and empty target counts used to calculate the dilution factor  
788 for inclusive elastic events; 3) statistical uncertainty in the ex-  
789 clusive  $ep \rightarrow e'\pi^+(n)$  channel due to limited statistics of car-  
790 bon and empty target data  $f_{\text{dil}}^{\pi} \pm (\text{stat.})$ ; and 4) the observed  
791 variation in  $P_b P_t f_{\text{dil}}^{\pi}$  when the input packing factor was var-  
792 ied within its uncertainty. The resulting total uncertainties on  
793  $P_b P_t f_{\text{dil}}^{\pi}$  were used for the evaluation of the uncertainty of  
794 the double-spin asymmetry  $A_{LL}$ . For the target asymmetry

795  $A_{UL}$ , the uncertainty was evaluated by combining the uncer-  
 796 tainty of  $P_b P_t f_{\text{dil}}^{\pi^+}$  and the uncertainty of the Møller measure-  
 797 ments on the beam polarization. The uncertainty from the  
 798 polarizations and the dilution is the largest systematic uncer-  
 799 tainty of the present analysis.

800 The uncertainty in the input packing factor of Table III was  
 801 checked using not only the  $W$  spectrum of elastic events (as  
 802 described in Section III D), but also the dilution factor of the  
 803  $en \rightarrow e'\pi^-(p)$  channel analyzed using a similar prescription  
 804 as Eqs. (40-42). The dilution factor of the  $\pi^-(p)$  channel  
 805 should be consistent with zero in all kinematic bins. Over-  
 806 all, the lower bound in the packing factor was cross-checked  
 807 between the  $en \rightarrow e'\pi^-(p)$  dilution result and the elastic  $W$   
 808 spectrum, and the upper bound in the packing factor was de-  
 809 termined always by the elastic  $W$  spectrum.

810 The kinematics dependence of the dilution factor on  $Q^2$ ,  $W$   
 811 and the pion center-of-mass angles  $\theta^*$  and  $\phi^*$  have been stud-  
 812 ied, and multi-dimensional fits of the dependence were per-  
 813 formed. The limited statistics of the carbon and the empty tar-  
 814 get data prevented fitting the  $(Q^2, W, \cos \theta^*, \phi^*)$  dependence  
 815 simultaneously. Instead, two bi-dimensional fits were used,  
 816 one for the  $(Q^2, W)$  dependence and one for the  $(\cos \theta^*, \phi^*)$   
 817 dependence, with the following ad-hoc parameterizations:

$$\begin{aligned} 818 \quad f_1 &= p_0 [1 + p_1(Q^2) + p_2(Q^2)^2] \\ 819 &\quad \times [1 + p_3(W - 1.8) + p_4(W - 1.8)^2] \\ 820 &\quad \times \left[1 + \frac{p_5}{(W^2 - 1.50^2)^2 + 1.50^2 \times 0.05^2}\right] \\ 821 &\quad \times \left[1 + \frac{p_6}{(W^2 - 1.68^2)^2 + 1.68^2 \times 0.05^2}\right] \quad (43) \end{aligned}$$

822 where  $W$  is in  $\text{GeV}/c^2$  and

$$\begin{aligned} 823 \quad f_2 &= p'_0 \times \left[1 + \frac{p_7}{1 - \cos \theta^*}\right] \\ 824 &\quad \times [1 + p_8 \sin \phi^* + p_9 \cos \phi^*] . \quad (44) \end{aligned}$$

825 The resulting two fits were then multiplied to give the over-  
 826 all  $2 \times 2$ -dimensional fit for  $f_{\text{dil}}^{\pi}(W, Q^2, \cos \theta^*, \phi^*)$ . To check  
 827 the validity of the fit, the results from  $f_{\text{dil}}^{\pi}(W, Q^2, \cos \theta^*, \phi^*)$   
 828 were integrated over 3 of the 4 variables, and then com-  
 829 pared with the dilution extracted directly from data binned  
 830 in the 4th variable. This comparison is shown in Fig. 12.  
 831 One can see that the dilution factors obtained from this  
 832 method agree with data very well. The  $2 \times 2$ -dimensional  
 833 fit  $f_{\text{dil}}^{\pi}(W, Q^2, \cos \theta^*, \phi^*)$  was used to correct the asymme-  
 834 tries  $A_{UL}$  and  $A_{LL}$  for the specific  $W, Q^2, \cos \theta^*, \phi^*$  bin us-  
 835 ing Eqs. (38-39).

### 837 G. Effect of Nitrogen Polarization on the Asymmetry

838 The  $^{15}\text{N}$  in the  $\text{NH}_3$  target is polarizable and can affect the  
 839 measured asymmetry. In this section we estimate this effect  
 840 and show that it is negligible. Therefore no correction was  
 841 made to the extracted exclusive channel asymmetries.

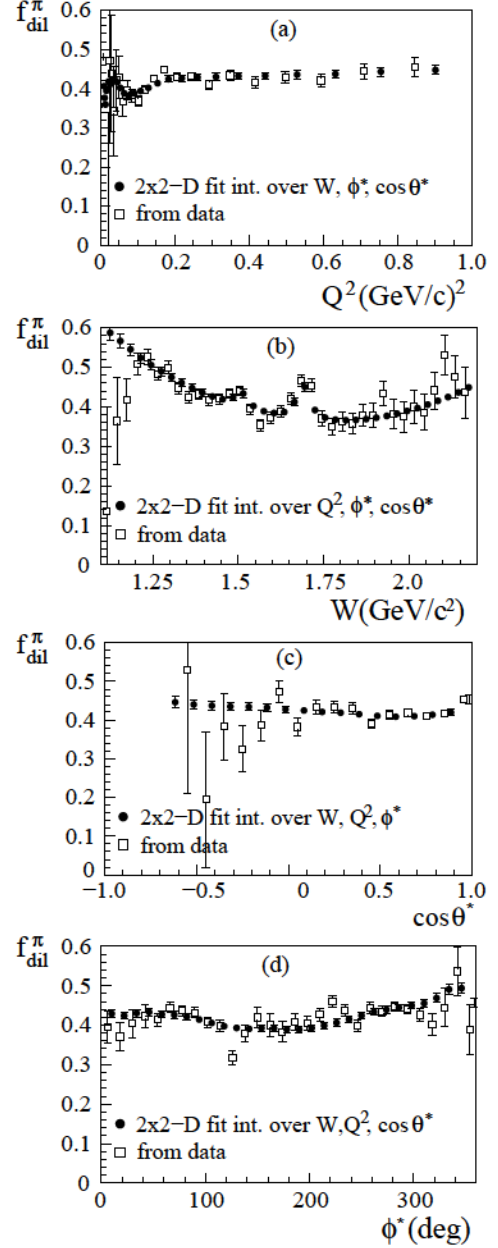


FIG. 12. Dependence of dilution on: (a)  $Q^2$ , (b)  $W$ , (c)  $\cos \theta^*$  and (d)  $\phi^*$ , for the  $3.0 \text{ GeV}$   $\text{NH}_3$  long top target,  $ep \rightarrow e'\pi^+(n)$  channel, obtained directly from the data (open squares) and from multiplying the two 2D fits of Eqs. (43-44) then integrating over 3 of the 4 variables (solid circles). The error bars for the dilution extracted from data are statistical only.

842 The nitrogen polarization in  $^{15}\text{NH}_3$  can be estimated based  
 843 on the Equal Spin Temperature (EST) prediction [39]:

$$844 \quad P(^{15}\text{N}) = \tanh \frac{\mu_{^{15}\text{N}} B}{k T_S}, P(\text{H}) = \tanh \frac{\mu_p B}{k T_S}, \quad (45)$$

845 where  $\mu_{^{15}\text{N}}$  and  $\mu_p$  are the magnetic moments of the  $^{15}\text{N}$  and  
 846 the proton, respectively,  $B$  is the magnetic field of the target,  $k$   
 847 is the Boltzmann constant and  $T_S$  is the spin temperature that  
 848 describes the Boltzmann distribution of spins inside the target.

TABLE III. Dilution factor  $f_{\text{dil}}^+$  and the product  $P_b P_t f_{\text{dil}}^+$  for the exclusive  $e^+ e^- \rightarrow e^+ e^- + \text{hadrons}$  channel. The  $P_b P_t$  results extracted from inclusive elastic scattering, described in section IIID, and their uncertainties are also shown. For  $P_b P_t$ , the three errors are due to statistical uncertainty of the elastic events, the statistical uncertainty of the carbon and empty target counts used to calculate the dilution factor for inclusive elastic analysis, and the uncertainty of the packing factor.  $P_b P_t$  values from Møller and NMR measurements are shown for comparison, although the NMR measurements are unreliable as described in section IIIC. The products  $P_b P_t f_{\text{dil}}$  are used to correct the exclusive channel asymmetries. The total uncertainties in  $P_b P_t f_{\text{dil}}$  include uncertainties of  $P_b P_t$ , statistical uncertainties of  $f_{\text{dil}}^+$ , and the uncertainties due to the packing factor (p.f.), all added in quadrature. These total uncertainties will be used as systematic uncertainties on the extracted exclusive channel asymmetries.

$E_{\text{beam}}$ (GeV)	Target (NH <sub>3</sub> )	p.f. (cm)	$(P_b P_t)_{\text{el}}$				Møller NMR	$f_{\text{dil}}^+$ (stat.)	(p.f.)	$P_b P_t f_{\text{dil}}$	$\frac{(P_b P_t f_{\text{dil}})}{P_b P_t f_{\text{dil}}}$ (total)	
3.0	top	0.65 0.05	0.614	0.006	0.015	0.045	0.620	0.424	0.021	0.013	0.260	7.0%
2.3	top	0.65 0.05	0.597	0.006	0.021	0.028	0.551	0.476	0.021	0.011	0.284	6.2%
	short	0.30 0.05	0.560	0.009	0.026	0.067	0.601	0.322	0.017	0.021	0.180	9.0%
2.0	top	0.65 0.05	0.605	0.004	0.016	0.030	0.545	0.495	0.020	0.010	0.299	5.7%
	bottom	0.65 0.05	0.636	0.019	0.016	0.031	0.560	0.484	0.021	0.010	0.308	6.4%
1.3	top	0.70 0.05	0.571	0.003	0.009	0.033	0.509	0.494	0.019	0.010	0.282	5.7%
	bottom	0.70 0.05	0.535	0.003	0.010	0.028	0.458	0.493	0.019	0.010	0.264	5.5%
	short	0.30 0.05	0.552	0.010	0.030	0.060	0.581	0.383	0.016	0.014	0.211	10.2%
1.1	bottom	0.75 0.10	0.568	0.002	0.007	0.080	0.563	0.496	0.020	0.020	0.282	11.1%

849 The EST prediction has been demonstrated to apply to the <sup>15</sup>N 878 on an event-by-event basis: instead of using the measured 850 and H of the ammonia molecule by several experiments start- 879 counts  $N$  , where each event counts as 1, we 851 ing with the Spin Muon Collaboration [52]. The SLAC E143 880 divided 1 by the acceptance of that particular event, then the 852 collaboration performed an empirical 881 sum was taken and used as  $N$  in the formula from 853 t and showed [53]:

$$853 P_{15\text{N}} = 0.136 P_p - 0.183 P_p^2 + 0.335 P_p^3 \quad (46)$$

854 which gives  $P_{15\text{N}} = 15\%$  when  $P_p = 90\%$  and  $P_{15\text{N}} = 8.8\%$  when  $P_p = 70\%$ . The <sup>15</sup>N polarization is carried 882 by the unpaired proton and its effect relative to the three free 883 protons in NH<sub>3</sub> is

$$858 P = \frac{1}{3} - \frac{1}{3} P^{(15\text{N})} \quad (47)$$

859 where the additional factor of  $1/3$  comes from the wave- 889 function of the unpaired proton in the <sup>15</sup>N [54]. The effect on 860 the asymmetry due to the polarized proton in the <sup>15</sup>N is thus at 890 the  $(1-2)\%$  level, and is negligible compared to the statistical 891 uncertainty of the asymmetry and the systematic uncertainty 892 due to the polarizations and the dilution factor.

## 865 H. Acceptance Corrections

866 When studying how the asymmetries vary with very small 888 bins in all four kinematic variables – the electron s  $Q^2$ ,  $W$  867 and the pion s center-of-mass angles  $\theta$  and  $\phi$  – the effect of 868 the detector acceptance and efficiency in principle cancel and 869 therefore do not affect the interpretation of the asymmetry re- 870 sults. The effect of acceptance only becomes relevant when 871 integration of the asymmetry over a subset of these four vari- 872 ables is necessary, which is the case for all results presented 873 in Section IV.

875 For results presented in Section IV, we evaluated the ac- 890 ceptance of each bin based on acceptance cuts for both elec- 891 trons and pions. The acceptance correction was then applied 892 to the extracted asymmetries.

## I. Radiative Corrections

893 Radiative corrections were calculated for both  $A_{UL}$  and 894  $A_{LL}$  using the code EXCLURAD [55] and the MAID2007 895 model [13]. It was found that overall the correction is fairly 896 small and typically no larger than 0.03. Considering the size 897 of the statistical uncertainty of the measurement, radiative cor- 898 rections were not applied to the asymmetries, but rather are 899 quoted as a systematic uncertainty of  $A = 0.03$  through- 900 out the accessed kinematics.

## J. Summary of All Systematic Uncertainties

899 The systematic uncertainty of the  $ep \rightarrow e^+ e^- + (n)$  exclu- 900 sive channel is dominated by that from the product  $P_b P_t f_{\text{dil}}^+$ , 901 shown in Table III. The uncertainty of  $P_b P_t f_{\text{dil}}^+$  takes into 902 account the uncertainties in the target packing factor, as well 903 as the thickness and density of various materials in the target. 904 Other non-negligible systematic uncertainties include a relative 905  $(1-2)\%$  due to the <sup>15</sup>N in NH<sub>3</sub> and a  $0.03$  due to radia-

TABLE IV. Summary of systematic uncertainties due to the target and beam polarizations and the dilution factor for different beam and target combinations. The (1–2)% relative uncertainty due to  $^{15}\text{N}$  and the 0.03 absolute uncertainty due to radiative corrections must be added in quadrature to the values here to obtain the total systematic uncertainty.

$E_{\text{beam}}$ (GeV)	Target ( $\text{NH}_3$ )	$A_{UL}$ (syst)	$A_{LL}$ (syst)
3.0	top	7.0%	7.0%
2.3	top	6.2%	6.3%
	short	9.0%	9.0%
2.0	top	5.7%	5.8%
1.3	top	5.7%	5.9%
	bottom	5.5%	5.7%
1.1	bottom	11.1%	11.2%

tive corrections. Adding these uncertainties in quadrature, we arrive at Table IV for our asymmetry results. For the asymmetry  $A_{UL}$ , one does not need to normalize by  $P_b$ . We relied on the elastic  $P_b P_t$  results and combined in quadrature their uncertainties with the uncertainty in the Møller polarization to obtain the uncertainty on  $P_t$  alone.

#### IV. ASYMMETRY RESULTS

Results for the target asymmetry  $A_{UL}$  and the double-spin asymmetry  $A_{LL}$  are available on a 4-dimensional grid of  $Q^2$ ,  $W$ ,  $\cos \theta$  and  $\phi$ . There are 42  $Q^2$  bins logarithmically spaced between 0.00453 and 6.45  $(\text{GeV}/c)^2$ , 38  $W$  bins between 1.1 and 2.21  $\text{GeV}/c^2$ , 30  $\cos \theta$  bins between 0 and 360, and 20  $\phi$  bins between  $-\pi$  and  $\pi$ . This binning scheme is referred to as “asymmetry bins”. To allow a meaningful comparison with theoretical calculations, we integrated the data over 3  $Q^2$  bins, 8  $W$  bins, 5  $\cos \theta$  bins and 5  $\phi$  bins. These will be referred to as “combined bins” hereafter. The resulting combined  $W$  bins are (1.1–1.34), (1.34–1.58) and (1.58–1.82)  $\text{GeV}/c^2$ , allowing an examination of the first, the second, and the third nucleon resonance regions, respectively.

The method of integrating the data for the combined bins was built upon the acceptance correction described in Section III H: to correct for the acceptance, each event in the asymmetry bin was divided by the acceptance of that particular event, then summed to be used as  $N$  in Eqs. (37–39). To integrate from asymmetry bins into combined bins, these acceptance-corrected  $N$  from each asymmetry bin was summed, and used as the combined  $N$  to evaluate the asymmetries for the combined bin. Using this method, the integrated asymmetries are direct predictions of the ratio of the physical cross sections integrated over the combined bin except for regions that had zero acceptance. To compare with theory, we calculated the cross sections for each asymmetry bin, then summed the calculated

cross sections over combined bins except for asymmetry bins where there was no data (zero acceptance). The ratio of the summed cross sections [Eqs. (20–21)] was taken as the calculated asymmetry for the combined bin. In the following we will present some representative results.

##### A. Results on Target Asymmetry $A_{UL}$

Figure 13 shows, in increasing  $Q^2$  ranges, the  $A_{UL}$  results as a function of  $W$  for three bins (120–180), (180–240), (240–300), and integrated over  $0.5 < \cos \theta < 1.0$ . Results for the  $\phi = (0^\circ, 60^\circ)$  and  $(300^\circ, 360^\circ)$  have less statistics and are not shown. Results for the  $\phi = (60^\circ, 120^\circ)$  bin have comparable statistics as Fig. 13 but are not shown here for brevity. In general, we see that the agreement between these  $A_{UL}$  results and the four calculations, MAID2007 (solid) [13], JANR (dashed) [14], SAID (dash-dotted) [15], and DMT2001 (dotted) [16], is very good in the  $W < 1.5$   $(\text{GeV}/c^2)$  region, but for the region  $1.5 < W < 1.8$   $(\text{GeV}/c^2)$ , all four calculations differ from each other and none agrees well with data, although the MAID2007 curve approximates the data better than the other three.

To study these results further for different  $W$  regions, we show in Fig. 14  $A_{UL}$  results as a function of  $W$  for three  $W$  ranges and between  $Q^2 = 0.0187$  and  $0.452$   $(\text{GeV}/c)^2$ . Results for lower  $Q^2$  ranges, down to 0.00646  $(\text{GeV}/c)^2$ , are available from the 1.1  $\text{GeV}$  data but only cover  $1.2 < W < 1.5$   $(\text{GeV}/c^2)$  and thus are not presented here. From Fig. 14, for the lower two  $W$  bins (1.12–1.34) and (1.34–1.58)  $\text{GeV}/c^2$ , the four calculations provide similar predictions and all agree with data. But for the  $W = (1.58–1.82)$   $\text{GeV}/c^2$  region, only the MAID2007 (solid) and the DMT2001 (dotted) calculations provide the correct sign, and MAID2007 approximates the data better than the other three although it does not agree with data perfectly. It is clear that all four calculations can be improved in the  $W > 1.58$   $\text{GeV}/c^2$  region throughout the  $Q^2$  range shown.

##### B. Results on the Double-Spin Asymmetry $A_{LL}$

Figure 15 shows the double-spin asymmetry  $A_{LL}$  results as a function of  $W$  for eight  $Q^2$  bins, three  $\cos \theta$  bins, and integrated over  $\phi = (0^\circ, 5^\circ, 10^\circ)$ . These results are compared with four calculations: MAID2007 (solid) [13], JANR (dashed) [14], SAID (dash-dotted) [15], and DMT2001 (dotted) [16]. Note that our definition for  $A_{LL}$  has opposite sign from theories, see Section IA. Results for the  $\phi = (0^\circ, 60^\circ)$  and  $(300^\circ, 360^\circ)$  bins have less statistics and are not shown. Results for the  $\phi = (60^\circ, 120^\circ)$  bin have comparable statistics as Fig. 13 but are not shown here for brevity. Overall the data agree very well with all four calculations. For all  $W$  bins, the sign of  $A_{LL}$  in the region of the  $N(1520)3^-2^-$  and the  $N(1680)5^-2^+$  is positive in the high  $Q^2$ , but start to cross or approach zero in the lower  $Q^2$  bin, within  $(0.0919, 0.156)$   $(\text{GeV}/c)^2$  for  $N(1520)3^-2^-$  and within  $Q^2 = (0.266, 0.452)$   $(\text{GeV}/c)^2$  for  $N(1680)5^-2^+$ , re-

993 spectively. This is in agreement with the suggestion in Sec- 1010  $W > 1.58 \text{ GeV } c^2$  where predictions from various models  
 994 tion I that  $A_{LL}$  turns to positive at high  $Q^2$  values due to 1011 differ signi cantly.  
 995 helicity conservation, but may become negative near the real  
 996 photon point.

1012

## ACKNOWLEDGMENTS

997

1013 The authors gratefully acknowledge the work of Jefferson  
 1014 Lab staff in the Accelerator and Physics Divisions that re-  
 998 We present here data on the target and double-spin asym- 1015 sulted in the successful completion of the experiment. This  
 999 metry  $A_{UL}$  and  $A_{LL}$  on the  $ep \rightarrow e^+(n)$  channel using data 1016 work was supported by: the U.S. Department of Energy  
 1000 taken on a polarized  $\text{NH}_3$  target, from the EG4 experiment us- 1017 (DOE), the U.S. National Science Foundation, the U.S. Jef-  
 1001 ferson CLAS in Hall B of Jefferson Lab. These data have reached 1018 fress Memorial Trust; the United Kingdom s Science and  
 1002 a low  $Q^2$  region from 0.0065 to 0.35  $(\text{GeV}/c)^2$  that was not ac- 1019 Technology Facilities Council (STFC) under grant num-  
 1003 cessed previously. They suggest a transition in  $A_{LL}$  from pos- 1020 bers ST/L005719/1 and GR/T08708/01; the Italian Istituto  
 1004 itive at higher  $Q^2$  to negative values below  $Q^2 = 0.1 (\text{GeV}/c)^2$  1021 Nazionale di Fisica Nucleare; the French Institut National de  
 1005 in the region  $1.5 < W < 1.7 \text{ GeV } c^2$ , in agreement with 1022 Physique Nucléaire et de Physique des Particules, the French  
 1006 both previous data from CLAS (high  $Q^2$ ) [20, 22] and the real 1023 Centre National de la Recherche Scienti que; and the Na-  
 1007 photon data at  $Q^2 = 0$ . Our results show that while all model 1024 tional Research Foundation of Korea. Jefferson Science As-  
 1008 calculations agree well with  $A_{LL}$ , in general there is room 1025 sociates, LLC, operates Jefferson Lab for the U.S. DOE under  
 1009 for improvements for  $A_{UL}$  in the high-mass resonance region 1026 U.S. DOE contract DE-AC05-060R23177.

1

1

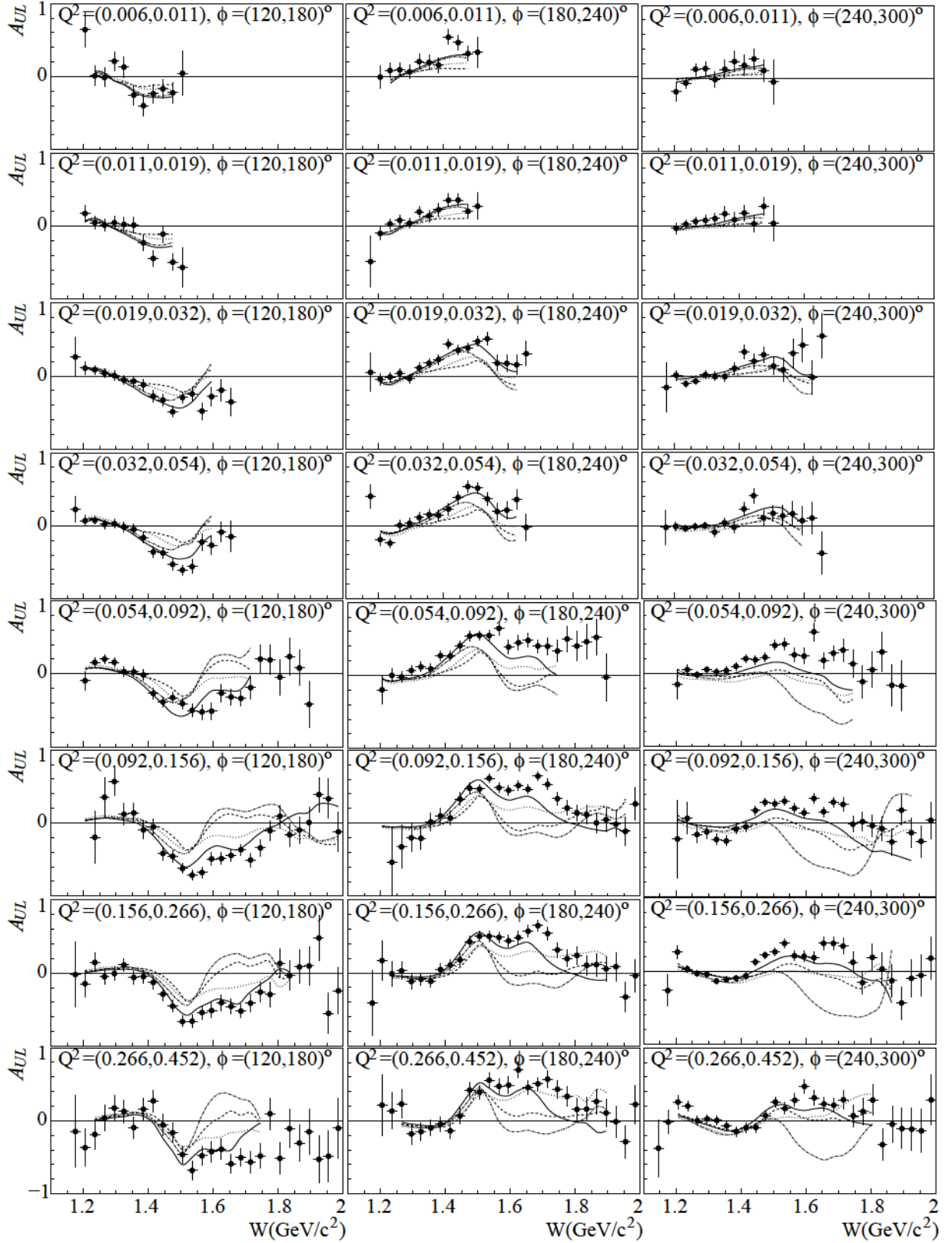


FIG. 13. Results on the target spin symmetries  $A_{UL}$  for the  $\bar{e}p \rightarrow e\pi^+(n)$  channel as a function of the invariant mass  $W$  in  $\text{GeV}/c^2$ , integrated over  $\cos\theta^* = (0.5, 1.0)$ , in increasing  $Q^2$  ranges and three  $60^\circ$   $\phi^*$  bins. From top to bottom the  $Q^2$  bins are  $(0.00646, 0.0110)$  and  $(0.0110, 0.0187)$  (1.1 GeV NH<sub>3</sub> long bottom target),  $(0.0187, 0.0317)$  and  $(0.0317, 0.054)$  (1.3 GeV NH<sub>3</sub> long top target),  $(0.054, 0.0919)$  (2.0 GeV NH<sub>3</sub> long top target),  $(0.0919, 0.156)$ ,  $(0.156, 0.266)$ , and  $(0.266, 0.452)$  ( $\text{GeV}/c^2$ ) (3.0 GeV NH<sub>3</sub> long top target). From left to right the  $\phi^*$  bins are  $\phi^* = (120^\circ, 180^\circ)$ ,  $(180^\circ, 240^\circ)$  and  $(240^\circ, 300^\circ)$ . In each panel, the horizontal scale is from 1.1 to 2  $\text{GeV}/c^2$  in  $W$  and the vertical scale is from  $-1$  to  $1$ . Data are compared to four calculations: MAID2007 (solid) [13], JANR (dashed) [14], SAID (dash-dotted) [15], and DMT2001 (dotted) [16].

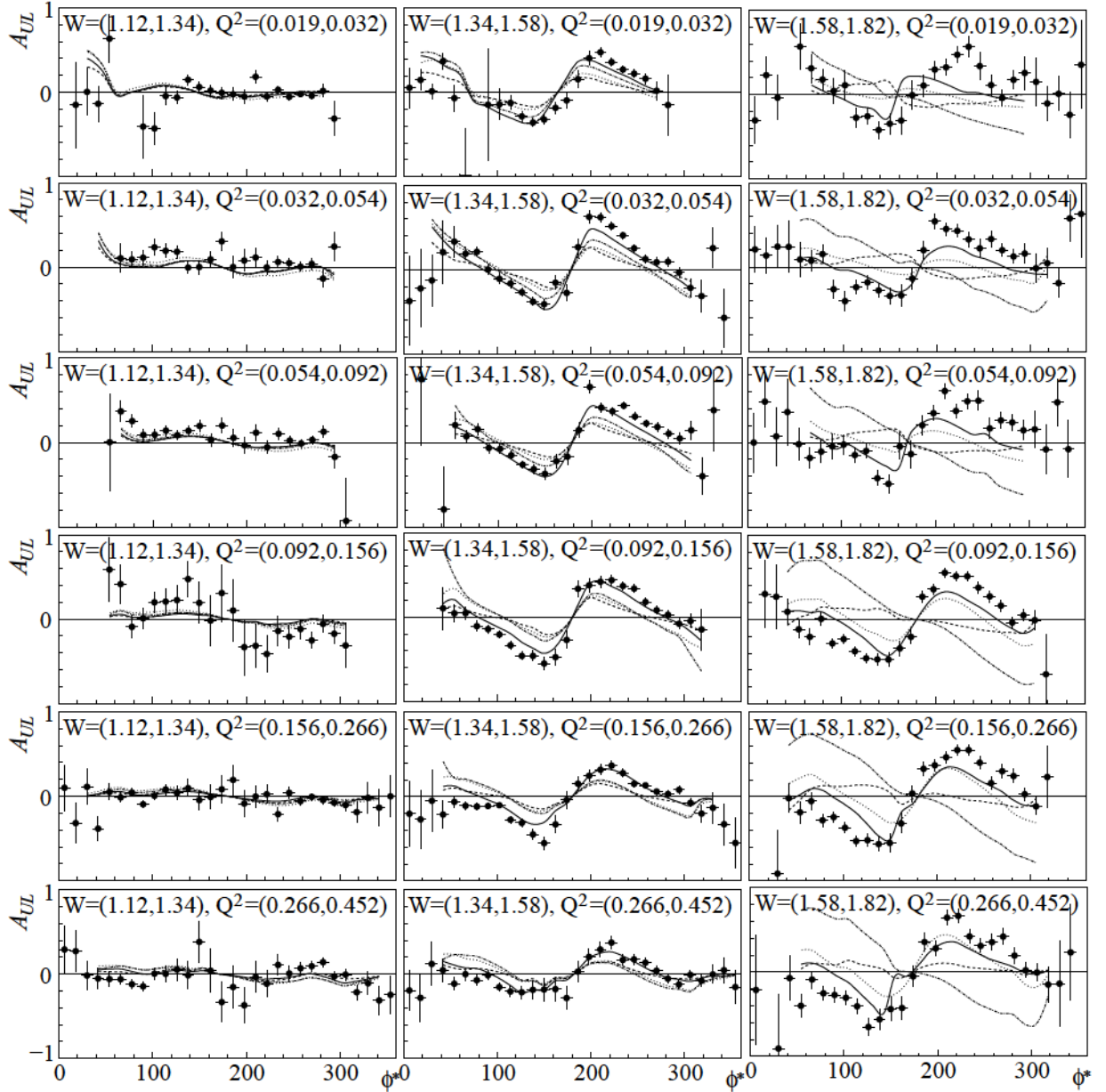


FIG. 14. Results on  $A_{UL}$  for the  $\bar{e}\bar{p} \rightarrow e\pi^+(n)$  channel as a function of azimuthal angle  $\phi^*$ , integrated over  $\cos\theta^* = (0.5, 1.0)$ , for six  $Q^2$  bins and three  $W$  bins. From top to bottom the six  $Q^2$  bins are:  $Q^2 = (0.0187, 0.0317)$  [1.3 NH<sub>3</sub> long target for  $W = (1.12, 1.34)$  and  $(1.34, 1.58)$  GeV/c<sup>2</sup>, and 2.0 NH<sub>3</sub> long top target for  $W = (1.58, 1.82)$  GeV/c<sup>2</sup>];  $(0.156, 0.266)$  and  $(0.266, 0.452)$  (GeV/c)<sup>2</sup> (2.0 GeV NH<sub>3</sub> long top target);  $(0.0919, 0.156)$ ,  $(0.156, 0.266)$  and  $(0.266, 0.452)$  (GeV/c)<sup>2</sup> (3.0 GeV NH<sub>3</sub> long top target); from left to right the  $W$  bins are:  $W = (1.12, 1.34)$ ,  $(1.34, 1.58)$ ,  $(1.58, 1.82)$  GeV/c<sup>2</sup>. In each panel, the horizontal scale is from 0 to 360° in  $\phi^*$  and the vertical scale is from -1 to 1. Data are compared to four calculations: MAID2007 (solid) [13], JANR (dashed) [14], SAID (dash-dotted) [15], and DMT2001 (dotted) [16].

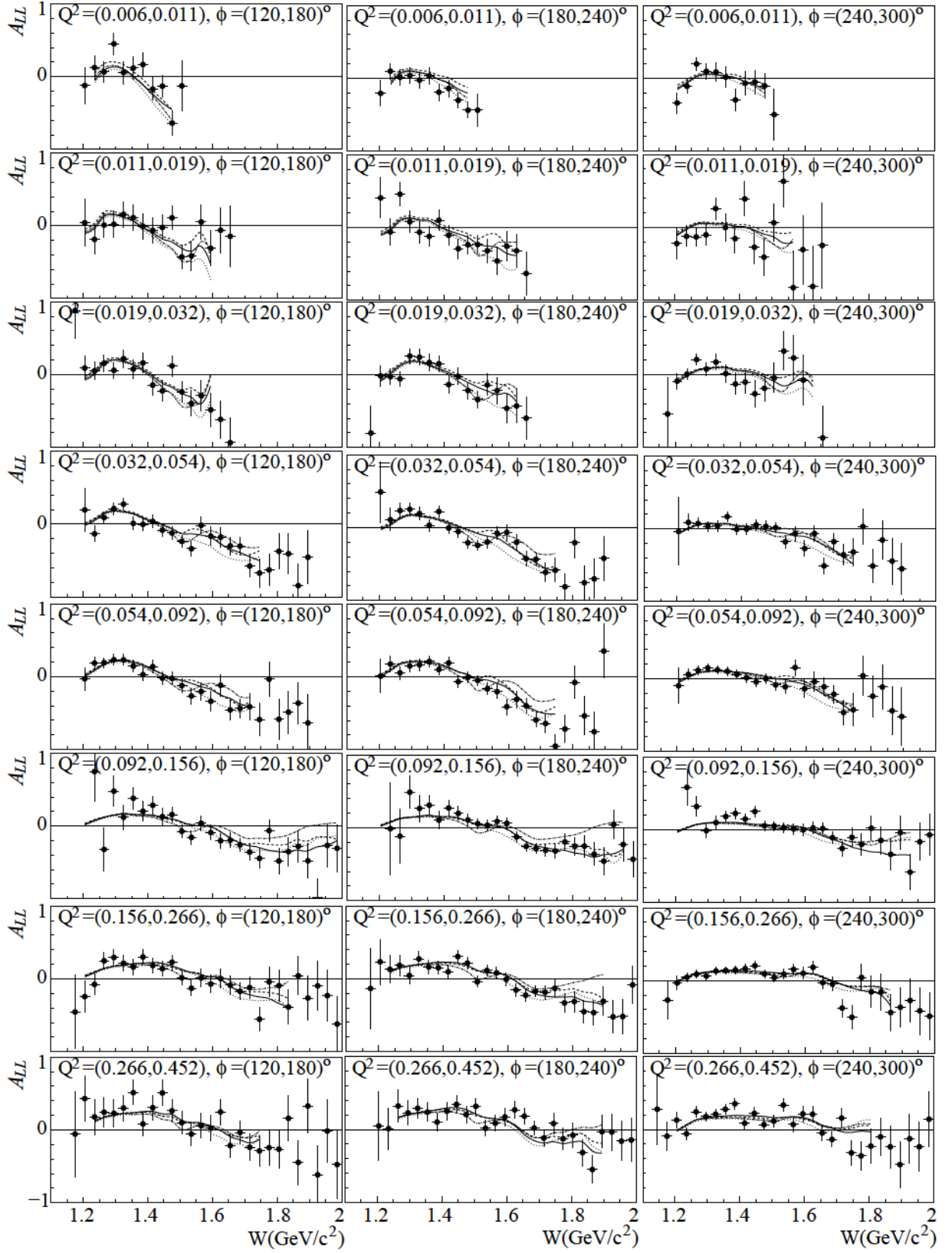


FIG. 15. Results on the double-spin symmetries  $A_{LL}$  for the  $e\vec{p} \rightarrow e\pi^+(n)$  channel as a function of the invariant mass  $W$  in  $\text{GeV}/c^2$ , integrated over  $\cos\theta^* = (0.5, 1.0)$ , for increasing  $Q^2$  ranges and three  $60^\circ$   $\phi^*$  bins. From top to bottom the  $Q^2$  bins are  $(0.00646, 0.011)$  and  $(0.011, 0.0187)$  (1.1 GeV NH<sub>3</sub> long bottom target),  $(0.0187, 0.0317)$  and  $(0.0317, 0.054)$  (1.3 GeV NH<sub>3</sub> long top target),  $(0.054, 0.0919)$  (2.0 GeV NH<sub>3</sub> long top target),  $(0.0919, 0.156)$ ,  $(0.156, 0.266)$ , and  $(0.266, 0.452)$  ( $\text{GeV}/c^2$ ) (3.0 GeV NH<sub>3</sub> long top target). From left to right the  $\phi^*$  bins are  $\phi^* = (120^\circ, 180^\circ)$ ,  $(180^\circ, 240^\circ)$  and  $(240^\circ, 300^\circ)$ . In each panel, the horizontal scale is from 1.1 to 2  $\text{GeV}/c^2$  in  $W$  and the vertical scale is from  $-1$  to  $1$ . Data are compared to four calculations: MAID2007 (solid) [13], JANR (dashed) [14], SAID (dash-dotted) [15], and DMT2001 (dotted) [16].

- 1027 [1] D. J. Gross and F. Wilczek, Phys. Rev. Lett. **30**, 1343 (1973). 1083  
 1028 [2] H. D. Politzer, Phys. Rev. Lett. **30**, 1346 (1973). 1084  
 1029 [3] V. D. Burkert and T. S. H. Lee, Int. J. Mod. Phys. E **13**, 1035 1085  
 1030 (2004). 1086  
 1031 [4] I. G. Aznauryan and V. D. Burkert, Prog. Part. Nucl. Phys. **67**, 1087  
 1032 1 (2012). 1088  
 1033 [5] C. Hoelbling, Acta Phys. Polon. B **45**, no. 12, 2143 (2014). 1089  
 1034 [6] A. Ukawa, J. Statist. Phys. **160**, 1081 (2015). 1090  
 1035 [7] V. Bernard, N. Kaiser, T. S. H. Lee and U. G. H. Meissner, Phys. 1091  
 1036 Rept. **246**, 315 (1994). 1092  
 1037 [8] V. Bernard, N. Kaiser and U. G. Meissner, Nucl. Phys. A **607**, 1093  
 1038 379 (1996) [Erratum-ibid. A **633**, 695 (1998)]. 1094  
 1039 [9] X. Zheng *et al.* [Jefferson Lab Hall A Collaboration], Phys. Rev. 1095  
 1040 Lett. **92**, 012004 (2004). 1096  
 1041 [10] X. Zheng *et al.* [Jefferson Lab Hall A Collaboration], Phys. Rev. 1097  
 1042 C **70**, 065207 (2004). 1098  
 1043 [11] M. Warns, W. Pfeil and H. Rollnik, Phys. Rev. D **42**, 2215 1099  
 1044 (1990). 1100  
 1045 [12] V. D. Burkert, R. De Vita, M. Battaglieri, M. Ripani and V. Mo- 1101  
 1046 keev, Phys. Rev. C **67**, 035204 (2003). 1102  
 1047 [13] D. Drechsel, S. S. Kamalov and L. Tiator, Eur. Phys. J. A **34**, 1103  
 1048 69 (2007). 1104  
 1049 [14] I. G. Aznauryan *et al.* [CLAS Collaboration], Phys. Rev. C **80**, 1105  
 1050 055203 (2009). 1106  
 1051 [15] The SAID partial wave analysis, R.A. Arndt *et al.*, URL: 1107  
 1052 <http://gwdac.phys.gwu.edu/>; R. A. Arndt, W. J. Briscoe, 1108  
 1053 M. W. Paris, I. I. Strakovsky and R. L. Workman, Chin. Phys. 1109  
 1054 C **33**, 1063 (2009). 1110  
 1055 [16] S. S. Kamalov and S. N. Yang, Phys. Rev. Lett. **83**, 4494 (1999). 1111  
 1056 [17] R. De Vita *et al.* [CLAS Collaboration], Phys. Rev. Lett. **88**, 1112  
 1057 082001 (2002) [Erratum-ibid. **88**, 189903 (2002)]. 1113  
 1058 [18] R. De Vita [CLAS Collaboration], Nucl. Phys. A **699**, 128 1114  
 1059 (2002). 1115  
 1060 [19] A. Biselli *et al.* [CLAS Collaboration], Phys. Rev. C **68**, 035202 1116  
 1061 (2003). 1117  
 1062 [20] J. Pierce, Double Spin Asymmetry in Exclusive + Electrop- 1118  
 1063 production with CLAS, Ph.D. thesis, University of Virginia (2008). 1119  
 1064 [21] S. Careccia, Single and Double Spin Asymmetries for Elec- 1120  
 1065 troproduction from the Deuteron in the Resonance Region, 1121  
 1066 Ph.D. thesis, Old Dominion University (2012). 1122  
 1067 [22] P. E. Bosted *et al.* [CLAS Collaboration], arXiv:1604.04350 1123  
 1068 [nucl-ex].  
 1069 [23] Particle Data Group, D.E. Groom *et al.*, Eur. Phys. J. C **15**, 1, 1125  
 1070 (2000).  
 1071 [24] S. Capstick, Phys. Rev. D **46**, 2864 (1992).  
 1072 [25] M. Gottschall *et al.* [CBELSA/TAPS Collaboration], Phys. Rev. 1128  
 1073 Lett. **112**, no. 1, 012003 (2014).  
 1074 [26] H. Iwamoto [CLAS Collaboration], AIP Conf. Proc. **1432**, 275 1130  
 1075 (2012).  
 1076 [27] D. Schott *et al.* [CLAS Collaboration], AIP Conf. Proc. **1735**, 1131  
 1077 030016 (2016).  
 1078 [28] JLab CLAS Experiment 04-102, D. I. Sober, M. Khandaker, 1132  
 1079 D. G. Crabb, *Helicity Structure of Pion Photoproduction*.  
 1080 [29] JLab CLAS Experiment 03-006, M. Battaglieri, R. De Vita, 1133  
 1081 A. Deur and M. Ripani, *The GDH Sum Rule with nearly real 1134  
 1082 photons and the proton  $g_1$  structure function at low momentum 1135  
 1083 transfer*.  
 1084 [30] JLab Proposal 05-111, A. Deur, G. Dodge and K. Slifer, *Mea- 1085  
 1086 surement of the Gerasimov-Drell-Hearn Integral at low  $Q_2$  on the Neutron and Deuteron*.  
 1087 [31] S. B. Gerasimov, Sov. J. Nucl. Phys. **2**, 430 (1966) [Yad. Fiz. **2**, 1088  
 1089 598 (1965)].  
 1090 [32] S. D. Drell and A. C. Hearn, Phys. Rev. Lett. **16**, 908 (1966).  
 1091 [33] M. Anselmino, B. L. Ioffe and E. Leader, Sov. J. Nucl. Phys. **49**, 136 (1989) [Yad. Fiz. **49**, 214 (1989)].  
 1092 [34] X. Ji, C. W. Kao and J. Osborne, Nucl. Phys. A **684**, 363 (2001).  
 1093 [35] Hyekoo Kang, Measurement of the proton spin structure func- 1094  
 1095 tions at very low momentum transfer, Seoul National University (2015).  
 1096 [36] B. A. Mecking *et al.* [CLAS Collaboration], Nucl. Instrum. 1097  
 1098 Meth. A **503**, 513 (2003).  
 1099 [37] G. Adams *et al.*, Nucl. Instrum. Meth. A **465**, 414 (2001).  
 1100 [38] E. Cisbani *et al.*, Nucl. Instrum. Meth. A **496**, 305 (2003).  
 1101 [39] D. G. Crabb and D. B. Day, Nucl. Instrum. Meth. A **356**, 9 (1995).  
 1102 [40] C. D. Keith *et al.*, Nucl. Instrum. Meth. A **501**, 327 (2003).  
 1103 [41] J. S. Price *et al.*, 5-MeV Mott polarimeter for rapid precise 1104  
 1105 electron beam polarization measurements, prepared for Conference: C96-09-10, p.727 Proceedings.  
 1106 [42] J. S. Price *et al.*, 5-MeV Mott polarimeter development at Jef- 1107  
 1108 ferson Lab, In Urbana 1997, Polarized gas targets and polarized 1109  
 1110 beams 446-450.  
 1111 [43] J. S. Price *et al.*, Recent measurements with the Jefferson Lab 5-MeV Mott polarimeter, In Protvino 1998, High energy spin 1112  
 1113 physics 554-556.  
 1114 [44] M. Steigerwald, MeV Mott polarimetry at Jefferson Lab, 1115  
 1116 [http://www.jlab.org/accel/inj\\_group/mott/mott.pdf](http://www.jlab.org/accel/inj_group/mott/mott.pdf)  
 1117 [45] K. Joo *et al.* [CLAS Collaboration], Phys. Rev. C **70**, 042201 (2004).  
 1118 [46] K. Park *et al.* [CLAS Collaboration], Phys. Rev. C **77**, 015208 (2008).  
 1119 [47] K. Adhikari, Measurement of the Spin Structure Function  $g_1^d$  1120  
 1121 of the Deuteron and Its Moments at Low  $Q^2$ , Ph.D. thesis, Old 1122  
 1123 Dominion University (2013).  
 1124 [48] CLAS-NOTE 2003-005, A. Klimenko and S. Kuhn, *Momentum Corrections for E6*.  
 1125 [http://www.jlab.org/Hall-B/notes/clas\\_notes03/03-005.pdf](http://www.jlab.org/Hall-B/notes/clas_notes03/03-005.pdf)  
 1126 [49] J. Beringer *et al.* (Particle Data Group), Phys. Rev. D **86**, 010001 (2012).  
 1127 [50] P. E. Bosted, Phys. Rev. C **51**, 409 (1995).  
 1128 [51] R. De Vita, *Measurement of the Double Spin Asymmetry in + Electroproduction with CLAS*, Ph.D. Thesis, Universita di Gen- 1129  
 1130 ova (2000).  
 1131 [52] B. Adeva *et al.* [Spin Muon Collaboration], Nucl. Instrum. 1132  
 1133 Meth. A **419**, 60 (1998).  
 1134 [53] K. Abe *et al.* [E143 Collaboration], Phys. Rev. D **58**, 112003 (1998).  
 1135 [54] O. A. Rondon-Aramayo, Phys. Rev. C **60**, 035201 (1999).  
 1136 [55] Radiative Corrections for Exclusive Reactions, A. Afanasev, 1137  
 1138 *et al*, Phys. Rev. D66, 074004, 2002; J. Gilfoyle *et al*, URL: <http://www.richmond.edu/ggilfoyl/research/RC/wvo.html>.